

# Identifying the Threshold Chain Length for Stress Overshoot in Ring-Linear Polymer Blends under Uniaxial Elongation: The Role of Multiple Threading

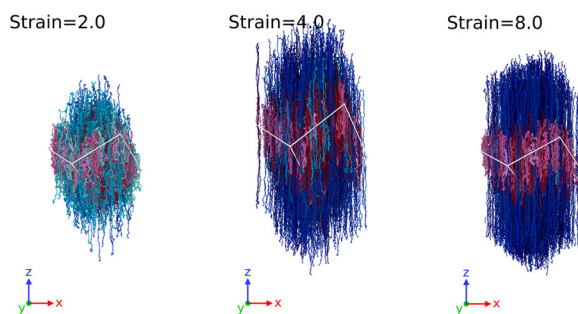
*Takahiro Murashima,<sup>\*1</sup> Katsumi Hagita,<sup>2</sup> and Toshihiro Kawakatsu<sup>1</sup>*

<sup>1</sup>Department of Physics, Tohoku University, 6-3, Aramaki-aza-Aoba, Aoba-ku, Sendai, 980-8578, Japan

<sup>2</sup>Department of Applied Physics, National Defense Academy, 1-10-20 Hashirimizu, Yokosuka, 239-8686, Japan

\*[murasima@cmpt.phys.tohoku.ac.jp](mailto:murasima@cmpt.phys.tohoku.ac.jp)

## Graphical Abstract



for Table of Contents use only (8.25cm x 4.45cm)

**ABSTRACT.** The rheological behavior of ring-linear polymer blends under uniaxial elongational flow has remained a subject of intense debate, particularly regarding the emergence of stress overshoot. Herein, we employ coarse-grained molecular dynamics simulations to investigate the

chain-length dependence of elongational viscosity in 1:1 ring-linear blends of flexible chains with the equal molecular weight. Our results reveal a distinct threshold in the degree of threading, quantified by the number of entanglements  $Z = N/N_e$  (where  $N$  is the number of beads per chain and  $N_e$  is the entanglement chain length), for the appearance of stress overshoot: while blends with shorter chains ( $Z \leq 2$ ) exhibit monotonic stress growth, a clear stress overshoot emerges when the chain length reaches a threshold value ( $Z \approx 4$ ). Consistent with previous reports, this overshoot originates from a thread-to-unthread transition. At the threshold chain length, multiple linear chains penetrate a single ring, providing sufficient topological constraints to significantly stretch the ring under elongational flow. We predict that this transition can be experimentally validated via 2D small-angle neutron scattering patterns in the plane of the stretching and perpendicular directions, offering a direct structural signature of the ring recoil process for future experimental verification.

## 1. Introduction

Ring polymers have remained a long-standing enigma in polymer physics due to their unique, end-free topology.<sup>1</sup> A major turning point in the history of this field was the landmark study by Kapnistos et al.<sup>2</sup> They demonstrated that the stress relaxation of high-purity ring polymer melts follows a power-law behavior distinct from the conventional reptation theory for linear chains.<sup>3</sup> To achieve the necessary purity, they utilized liquid chromatography at the critical condition<sup>4</sup> (LCCC), which enabled the efficient separation of topologically pure rings from linear chain contaminants. They further experimentally revealed that even a trace amount of linear chain contaminants can lead to the “threading” of rings by linear chains, creating a “pinning” effect that dramatically retards the relaxation dynamics. Since this discovery, elucidating the

microscopic nature of these topological constraints—specifically how threading events dictate the size and diffusivity of the rings—has been a subject of intensive research using molecular simulations<sup>5–10</sup> and, more recently, advanced neutron scattering techniques.<sup>11,12</sup> In parallel, numerous studies have highlighted the complex rheological consequences of such interactions, identifying a non-monotonic dependence of viscosity on blend composition where the mixture viscosity can even surpass that of the pure linear counterpart.<sup>13–16</sup>

In equilibrium and linear response regimes, these topological constraints cause the rings to become trapped within the entanglement network of the surrounding linear chains. These trapped rings can only relax through constraint release induced by the motion of the linear chains, which leads to a dramatic increase in the blend viscosity.<sup>15</sup> Furthermore, recent coarse-grained molecular dynamics simulations have reported that the threading between ring and linear chains forms a composite entanglement topology, which acts as an additional source of friction under non-linear flow conditions.<sup>17</sup> Direct evidence for such intermittent topological interactions has been provided by single-molecule observations. Zhou et al.<sup>18,19</sup> used fluorescence microscopy to visualize the dynamics of individual ring DNA molecules in semidilute linear DNA solutions under extensional flow. They discovered that rings exhibit strikingly large conformational fluctuations even in the steady-state regime, which they attributed to the transient threading and unthreading of linear chains through the stretched rings. These molecular-scale observations strongly support the idea that the coupling between ring and linear components is governed by a dynamic topological process.

The most singular phenomenon in uniaxial elongational flow is the emergence of a stress overshoot in the transient elongational viscosity. Borger et al.<sup>20</sup> identified that this overshoot is driven by a “thread-to-unthread” transition. Immediately after the start-up of uniaxial elongation,

the threaded linear chains act as moving pulleys, forcibly stretching the ring chains and causing an accumulation of excessive tension within them. Subsequently, as the strain increases, the linear chains unthread from the rings, leading to a sudden release of the accumulated tension, which is observed macroscopically as a stress drop (overshoot).

However, it has been suggested that the presence or absence of this overshoot phenomenon strongly depends on the number of entanglements per chain,  $Z$ . The systems for which clear overshoots under uniaxial elongation have been reported—including the experiments and simulations of Borger et al.<sup>20</sup> and the large-scale simulations of O'Connor et al.<sup>17</sup>—all utilized sufficiently long chains with  $Z \approx 14$ . In contrast, we showed in our previous work<sup>21</sup> that for ring-linear blends of flexible chains with  $Z \approx 2$ , a prominent overshoot was observed in biaxial elongational flow, whereas no such overshoot was detected under uniaxial elongational flow. Since it remained unclear whether this absence was due to the inherent nature of flexible chains or simply an insufficient degree of entanglement, investigating the emergence of an overshoot in longer flexible systems is of fundamental importance. These collective results suggest that a threshold chain length is required to generate a powerful “topological grip”<sup>21</sup> that is sufficient to overstretch the rings and induce a macroscopic stress peak under uniaxial elongation. Furthermore, previous analyses have shown that as the size of the ring chain increases, the number of penetrating linear chains ( $n_p$ ) also increases, which induces the expansion of the ring conformation.<sup>5–11</sup> This strongly suggests that if the chain length is sufficiently long, a “multiple threading” state—where multiple linear chains interact with a single ring—is formed, potentially producing a more strong stretching effect under elongation.

In this study, we perform coarse-grained molecular dynamics simulations of ring-linear homopolymer blends with the equal molecular weight. By systematically varying the chain

length ( $Z = 1, 2,$  and  $4$ ), we investigate the chain-length dependence of the non-linear elongational rheology. Specifically, we focus on the transition from the unentangled to the moderately entangled regime to clarify whether a critical chain length exists for the emergence of a macroscopic stress overshoot. Our analysis aims to elucidate the role of multiple threading and how the number of topological constraints dictates the transient conformational tension of the rings under strong flow conditions. By combining stress decomposition, topological analysis using the Gauss linking number, and real-space density profiles, we provide a consistent physical picture of how multiple threading dictates the non-linear signatures of ring-linear blends. Furthermore, we predict the 2D small-angle neutron scattering (SANS) patterns in the plane of the stretching and perpendicular directions associated with this transition, offering a roadmap for future experimental validation using elongational rheometers coupled with neutron beamlines.

## 2. Simulation Method

We employed the coarse-grained bead-spring model developed by Kremer and Grest<sup>22</sup> to simulate the dynamics of ring-linear polymer blends. In this model, all beads interact via the truncated-and-shifted Lennard–Jones (LJ) potential, which accounts for excluded volume effects. Adjacent beads along a chain are connected by the finite extensible nonlinear elastic (FENE) potential. For the flexible Kremer–Grest model (with no bending potential), previous estimates of the entanglement length have varied between  $N_e = 65$  and  $85$ , depending on the specific topological analysis method and finite chain length effects.<sup>23–27</sup> Recent comprehensive studies,<sup>28–30</sup> however, have provided more refined estimates by accounting for long-range bond correlations induced by melt incompressibility and by employing  $N \rightarrow \infty$  extrapolation to eliminate systematic errors associated with chain ends. Following these advancements, which

identify  $N_e \approx 80$  as the asymptotic limit for properly equilibrated, long-chain flexible melts, we adopt  $N_e = 80$  as the characteristic entanglement length in this study. We investigated equi-weight (1:1 ratio) blends of ring and linear polymers with identical chain lengths of  $N = 80, 160,$  and  $320$ , which correspond to  $Z = 1, 2,$  and  $4$ , respectively. The choice of the equi-weight composition is based on the findings of O'Connor et al.,<sup>17</sup> who explored various ring-linear mixing ratios and reported that the magnitude of the stress overshoot is maximized in the 1:1 blend. This composition is also of particular experimental interest; Kruteva et al.<sup>12</sup> recently demonstrated that the zero-shear viscosity of symmetric ring-linear blends reaches a maximum at the 1:1 blend, where the ring dynamics undergo a distinct crossover from self-similar relaxation to a regime governed by the linear entanglement network. By selecting this ratio, we aim to capture the most prominent rheological signatures of the topological interactions between the two components. The total number of particles in each simulation was  $N_{\text{tot}} = 614,400$  for all chain lengths considered ( $N = 80, 160,$  and  $320$ ). For comparison, pure linear and pure ring melts were also simulated as baseline systems.

All physical quantities are reported in standard LJ units, where the bead diameter  $\sigma$ , the depth of the LJ potential well  $\varepsilon_{\text{LJ}}$ , and the bead mass  $m$  are set to unity. The characteristic time scale is defined as  $\tau = \sigma \sqrt{\frac{m}{\varepsilon_{\text{LJ}}}}$ . The system temperature was maintained at  $T = 1.0 \frac{\varepsilon_{\text{LJ}}}{k_{\text{B}}}$ . For both the equilibrium and non-equilibrium molecular dynamics (NEMD) simulations under uniaxial elongation, we consistently employed Langevin dynamics with a damping parameter of  $2.0\tau$ , corresponding to a friction coefficient of  $\gamma = 0.5\tau^{-1}$ , to maintain a stable isothermal condition. The monomer density was set to  $\rho = 0.85\sigma^{-3}$ . In the FENE potential, for bonded interactions, the spring force constant  $k = 30 \frac{\varepsilon_{\text{LJ}}}{\sigma^2}$  and the maximum bond extension length  $R_0 = 1.5\sigma$ . For non-bonded interactions, the truncated-and-shifted LJ potential with a cut-off distance of  $r_{\text{cut}} = 2^{1/6}\sigma$

acts as a purely repulsive potential. Given the number density  $\rho$ , the volume of the simulation box is  $V = N_{\text{tot}} / \rho$ , resulting in a cubic box length of  $L = V^{1/3} \approx 89.8\sigma$ . This system size was chosen to ensure that the cubic simulation box length is well exceeds not only the radius of gyration ( $R_g = 9.4\sigma$ ) but also the mean end-to-end distance ( $R_{\text{ee}} = 22.1\sigma$ ) for linear chains in the blend with  $N = 320$ . By maintaining  $L > 4R_{\text{ee}}$ , we preclude unphysical interactions between a chain and its own periodic images. Most importantly, by employing the generalized Kraynik-Reinelt boundary conditions<sup>31–35</sup> described below, this volume is sufficient to avoid such self-interactions even under uniaxial elongational flow. For the system studied here, we confirmed that the distance to self-periodic images was greater than  $20\sigma$  even at the maximum Hencky strain of  $\epsilon = 10$ .

The systems were first equilibrated using Langevin dynamics at a constant temperature ( $T = 1.0 \frac{\epsilon_{\text{LJ}}}{k_{\text{B}}}$ ). NEMD simulations were then performed to investigate the response under uniaxial elongational flow. The flow field was imposed by integrating the SLLOD equations of motion.<sup>36</sup> In standard elongational flow simulations, the simulation box rapidly contracts in the perpendicular directions, limiting the maximum achievable strain. To overcome this, we utilized the UEF package<sup>33</sup> and its extension for Langevin dynamics (UEFEX package),<sup>35</sup> which implements the generalized Kraynik–Reinelt boundary conditions<sup>31,32</sup> for long-time uniaxial deformation. The key strategy is the use of a triclinic simulation cell where the initial lattice vectors are tilted at a specific angle relative to the principal elongation axis.<sup>31,32</sup> By periodically re-mapping the deforming box back to its original tilted geometry—a technique conceptually similar to the original Kraynik–Reinelt boundary conditions<sup>37–39</sup>—the simulation can be continued indefinitely without the box dimensions ever falling below a critical threshold. This numerical “trick” enables us to maintain a consistent periodic boundary condition in all

directions while imposing a constant strain rate up to very large Hencky strains ( $\epsilon \geq 6$ )<sup>34,35</sup>, enabling the full observation of the thread-to-unthread transition in ring-linear blends.

The range of the imposed Hencky strain rates  $\dot{\epsilon} \equiv \frac{d\epsilon}{dt}$  was selected to span the non-linear rheological regime, specifically within the interval  $\frac{1}{\tau_d} \lesssim \dot{\epsilon} \lesssim \frac{10}{\tau_e}$ , where  $\tau_d$  and  $\tau_e$  represent the longest relaxation time for chain reconfiguration (the disengagement time) and the relaxation time of segments between entanglement points (the entanglement time), respectively. In our model of flexible Kremer–Grest chains, the entanglement time is estimated to be  $\tau_e \approx 8000\tau$ , which corresponds to  $\tau_d$  of  $Z = 1$  ( $N = 80$ ), while the values for the longest relaxation time  $\tau_d$  for each blend will be discussed and estimated in the following results section based on the orientational relaxation of the chain.<sup>35</sup> The selection of this range was also guided by numerical stability and precision requirements. For very high strain rates approaching or exceeding  $\frac{10}{\tau_e}$  (ten times the reciprocal of the entanglement time scale), we observed a significant rise in the system temperature due to intense artificial viscous heating, which complicates the maintenance of a stable isothermal state.<sup>35</sup> Furthermore, at lower strain rates near or below  $\frac{1}{\tau_d}$ , the signal-to-noise ratio in the stress measurements becomes increasingly problematic, with large relative fluctuations in the transient stress making it difficult to resolve the fine features of the stress-strain curves.

Simulations were performed using HOOMD-blue<sup>40</sup> on GPUs for equilibrium analysis and LAMMPS<sup>41,42</sup> for non-equilibrium analysis. Molecular snapshots and visualizations were generated using OVITO.<sup>43</sup> To improve the signal-to-noise ratio in the transient stress measurements, the time-evolution data of the stress were smoothed using a Savitzky–Golay filter.<sup>44</sup>

### 3. Results

#### 3.1. Linear Viscoelasticity and Relaxation Time

To establish the baseline rheological properties, we first examined the linear viscoelasticity of the ring-linear blends. **Figure 1** shows the shear relaxation modulus  $G(t)$  for  $N = 80, 160,$  and  $320$  ( $Z = 1, 2,$  and  $4,$  respectively). The shear relaxation modulus was calculated from the equilibrium stress fluctuations using the Green–Kubo relation.<sup>45</sup> To ensure high statistical precision even in the terminal relaxation regime, we employed the multiple-tau correlator method proposed by Ramírez et al.,<sup>46</sup> which allows for the efficient computation of the stress autocorrelation function over a wide range of time scales. A striking contrast is observed between the pure ring melts and the blends. The pure ring melts exhibit the fastest relaxation because ring polymers in their pure state cannot form conventional entanglements. In the intermediate time regime, the stress relaxation of these pure rings follows a power-law behavior with a power of  $1/2$ , which can be understood simply as a manifestation of the self-similarity of Rouse chains. This power-law decay persists until the whole ring relaxes, leading into the terminal relaxation regime. According to experimental studies on pure ring polymer melts by Doi et al.,<sup>47,48</sup> the behavior of the shear relaxation modulus for systems with up to approximately  $Z \approx 5$  can be well approximated by the Rouse ring model.

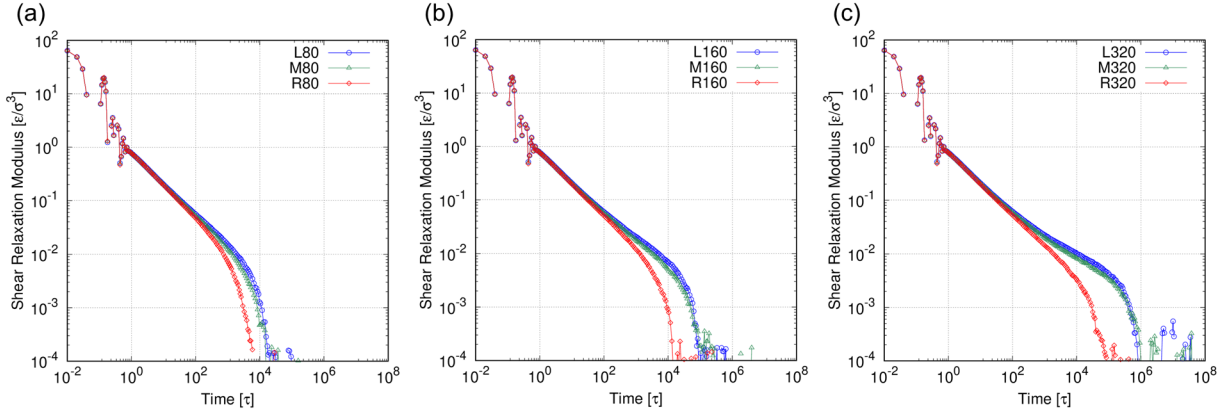


**Figure 1.** Shear relaxation modulus  $G(t)$  as a function of time for (a)  $N = 80$ , (b)  $N = 160$ , and (c)  $N = 320$ . Each panel compares the linear melt (L), ring melt (R), and equi-weight ring-linear blend (M). The data were obtained from equilibrium coarse-grained molecular dynamics simulations using the Green–Kubo relation.

For the equi-weight blends, the relaxation behavior is remarkably similar to that of the pure linear melts. This behavior is consistent with previous experimental and simulation studies.<sup>2,14</sup> Specifically, for the systems with  $N = 160$  and  $320$  ( $Z = 2$  and  $4$ ), the stress relaxation evolves from an initial Rouse-like power-law to a transient entanglement plateau before entering the terminal regime. This emergence of the plateau reflects the recovery of topological constraints: the threading of linear chains through the rings creates an effective entanglement network between the ring and linear components.<sup>17</sup> Consequently, the dynamics of the ring polymers are significantly retarded, becoming comparable to the relaxation of the linear chains as the threaded rings are effectively trapped within the matrix entanglements.

The characteristic relaxation times  $\tau_d$  were determined by calculating the time correlation functions of characteristic vectors specific to the linear and ring architectures as follows. For

linear chains, the correlation function of the end-to-end vector was used. For ring polymers, we calculated the correlation function of the diameter vector, defined as the vector connecting beads 1 and  $N/2$  along the ring. The resulting correlation functions were fitted with the Kohlrausch-Williams-Watts function to estimate the characteristic relaxation times, following the procedure described in our previous work.<sup>35</sup> These estimated relaxation times are summarized in **Table 1**. As shown in **Figure 2**, the relaxation times of each component exhibit distinct dependencies on chain length. The relaxation time of the linear component in the blend ( $\tau_{d,M,L}$ ) remains nearly identical to that of the pure linear melt ( $\tau_{d,L}$ ), suggesting that the linear entanglement network is not significantly altered by the presence of rings at this composition. In contrast, while the relaxation time of the ring component in the blend ( $\tau_{d,M,R}$ ) is relatively close to that of the pure ring melt ( $\tau_{d,R}$ ) at small  $N$ , it deviates significantly as  $N$  increases. For the longest chain length ( $N = 320$ ,  $Z \approx 4$ ),  $\tau_{d,M,R}$  shows a pronounced increase, becoming several times longer than  $\tau_{d,R}$  and approaching the value of  $\tau_{d,L}$ . This trend indicates that as the chain length increases, the rings become more effectively trapped by the multiple threading of linear chains, causing their dynamics to be increasingly constrained by the surrounding linear entanglement network. Comparing the data for  $N = 160$  and  $N = 320$  in **Table 1**,  $\tau_{d,R}$  increases by a factor of 4, whereas  $\tau_{d,M,R}$  increases by nearly a factor of 10. This signifies that the relaxation time of pure rings follows a scaling of  $N^2$ , while that of the rings in the ring-linear blend scales as  $N^3$ . These results are qualitatively consistent with the findings reported by Mo et al.,<sup>10</sup> who investigated the dynamics of tracer rings in linear matrices.

**Table 1.** Relaxation times for linear chains and rings in pure melts ( $\tau_{d,L}$  and  $\tau_{d,R}$ ), and blends ( $\tau_{d,M,L}$  and  $\tau_{d,M,R}$ ). The entanglement time  $\tau_e \approx 8000\tau$  was estimated from the value of  $\tau_{d,L80}$ .

	$N = 80$	$N = 160$	$N = 320$
$\tau_{d,L}$	$7994\tau$	$48111\tau$	$505913\tau$
$\tau_{d,R}$	$1755\tau$	$6708\tau$	$26620\tau$
$\tau_{d,M,L}$	$7664\tau$	$49874\tau$	$497830\tau$
$\tau_{d,M,R}$	$2386\tau$	$12977\tau$	$116925\tau$

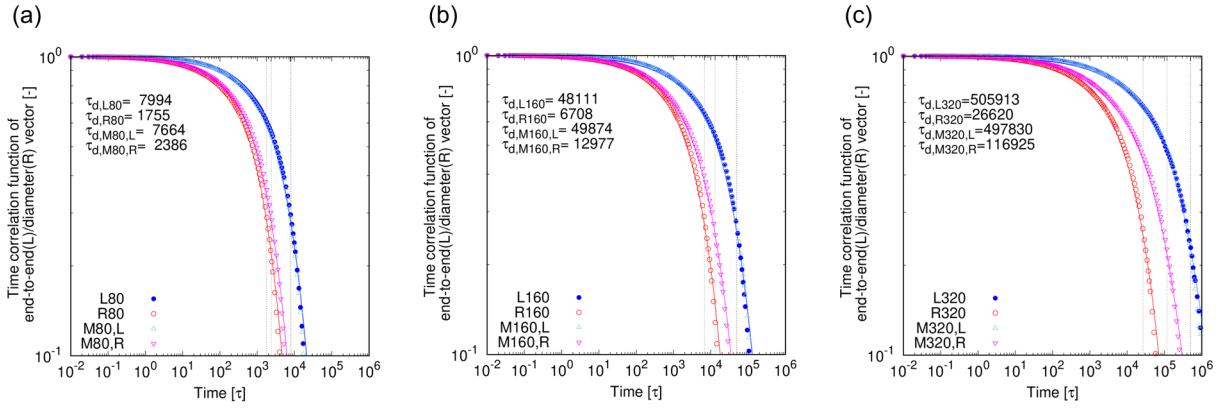


**Figure 2.** Time correlation functions of the end-to-end vector for linear chains (L) and the diameter vector for ring polymers (R) at (a)  $N = 80$ , (b)  $N = 160$ , and (c)  $N = 320$ . The characteristic relaxation times ( $\tau_d$ ) are indicated for each component in the pure melts and blends. The components in the blends are designated as  $MN,L$  and  $MN,R$ , corresponding to the linear and ring chains of length  $N$ .

### 3.2. Elongational Rheology

The non-linear rheological response of the ring-linear blends was investigated under uniaxial elongational flow. **Figure 3** shows the transient elongational viscosity  $\eta_E(t) = N_1(t)/\dot{\epsilon}$  as a function of time for various strain rates  $\dot{\epsilon}$ , where  $N_1(t) = \sigma_{zz}(t) - 0.5[\sigma_{xx}(t) + \sigma_{yy}(t)]$  is the first normal stress difference. A key finding of this study is the emergence of a distinct threshold in

chain length for the appearance of stress overshoot in these blends. To evaluate the degree of non-linearity, we also plot the linear viscoelastic envelope  $3\eta(t)$ . This baseline is calculated from the shear relaxation modulus  $G(t)$  obtained at equilibrium (shown in **Figure 1**) as:  $3\eta(t) = 3 \int_0^t G(s) ds$ . In the limit of small strains or low strain rates,  $\eta_E(t)$  is expected to follow the  $3\eta(t)$  curve, consistent with Trouton's ratio.<sup>49</sup>

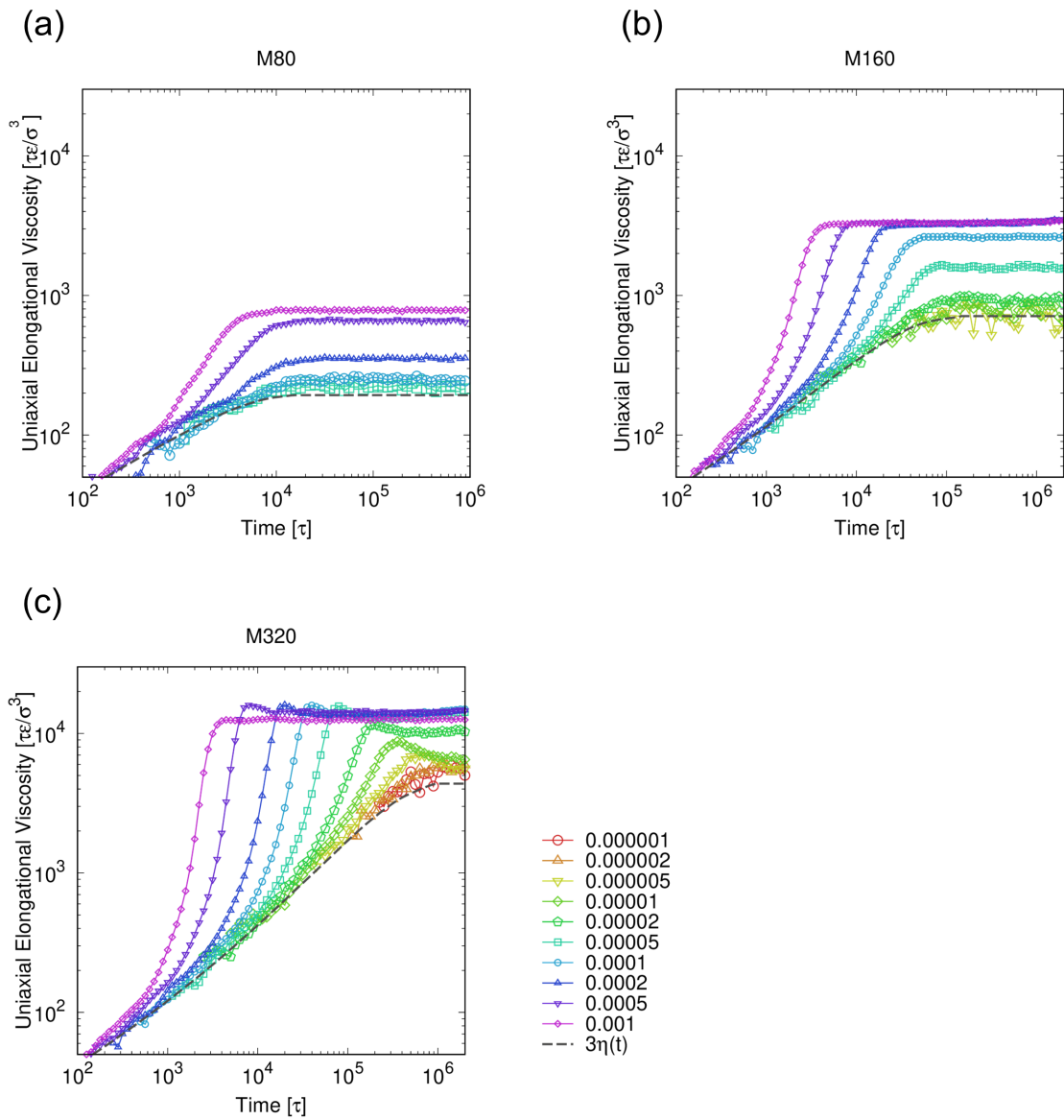


**Figure 3.** Transient uniaxial elongational viscosity  $\eta_E(t)$  at various strain rates  $\dot{\epsilon}$  for (a) M80 ( $N = 80, Z = 1$ ), (b) M160 ( $N = 160, Z = 2$ ), and (c) M320 ( $N = 320, Z = 4$ ). A common legend is used for all three panels, where the symbols and their corresponding numerical values denote the applied strain rates,  $\dot{\epsilon}$  [ $1/\tau$ ]. The dashed line represents  $3\eta(t)$ , which serves as the linear viscoelastic envelope. The distinct stress overshoots are observed only for the M320 case when  $\dot{\epsilon} > 1/\tau_d$ , identifying the threshold chain length for non-linear extensional rheology.

As the strain rate increases and exceeds the reciprocal of the longest relaxation time ( $Wi > 1$  or  $\dot{\epsilon} > 1/\tau_d$ , where  $Wi = \dot{\epsilon} \tau_d$  is the Weissenberg number), all systems started to exhibit significant strain hardening, where the elongational viscosity grows rapidly beyond the linear  $3\eta(t)$  envelope. However, the subsequent qualitative behavior depends strongly on the chain length. For the blends with shorter chains, M80 ( $N = 80, Z = 1$ ) and M160 ( $N = 160, Z = 2$ ), the elongational viscosity exhibits monotonic growth followed by a steady state, as shown in **Figures 3a and b**. Even at high strain rates where the chains are expected to be significantly deformed and stretched, no macroscopic stress overshoot was observed in the total stress of these systems. In sharp contrast, the M320 blend ( $N = 320, Z = 4$ ) displays a clear and pronounced stress overshoot following the initial strain hardening, as shown in **Figure 3c**. This transition from monotonic growth to overshoot behavior as the chain length increases from  $Z = 2$  to 4 identifies  $Z \approx 4$  as the threshold degree of threading required to trigger non-linear stress signatures in ring-linear blends. This threshold suggests that a minimum number of topological constraints—specifically, multiple threading of linear chains through a single ring—is necessary to sustain a sufficiently high conformational tension that can be rapidly released upon unthreading, leading to the observed stress peak. Following this logic, one would expect the stress overshoot to be even

more pronounced in systems with higher degrees of entanglement. To test this, we further examined the case of  $Z = 8$  ( $N = 640$ ) and indeed observed a clear stress overshoot (**Figure S1** in the Supporting Information), as expected. These results collectively demonstrate that the stress overshoot is not a phenomenon exclusive to specific chain architectures or rigidities, but can be clearly manifested even in flexible chain systems once the degree of entanglement exceeds a certain threshold.

To further clarify the molecular origin of the stress overshoot observed for the M320 blend ( $N = 320$ ,  $Z = 4$ ), we decomposed the total first normal stress difference  $N_1$  into the contributions of the ring and linear components. **Figure 4** shows this decomposition as a function of Hencky strain  $\epsilon = \dot{\epsilon}t$  at various strain rates  $\dot{\epsilon}$ . As shown in **Figure 4a**, the total stress exhibits a peak before reaching a steady state, particularly at higher strain rates. The decomposition reveals that this overshoot behavior is primarily driven by the ring component, as shown in **Figure 4b**. The stress contribution from the rings increases sharply, reaches a distinct maximum at a Hencky strain of 3–4, and then significantly relaxes. Notably, this peak is more clearly observable at intermediate strain rates rather than the highest one. This occurs because, at lower strain rates, the flow-induced constraints are less dominant, allowing the rings to relax more effectively. Consequently, the stress peak stands out more prominently than at the highest rate. In contrast, as shown in **Figure 4c**, the linear component exhibits a monotonic increase in stress followed by a plateau, with no detectable overshoot.

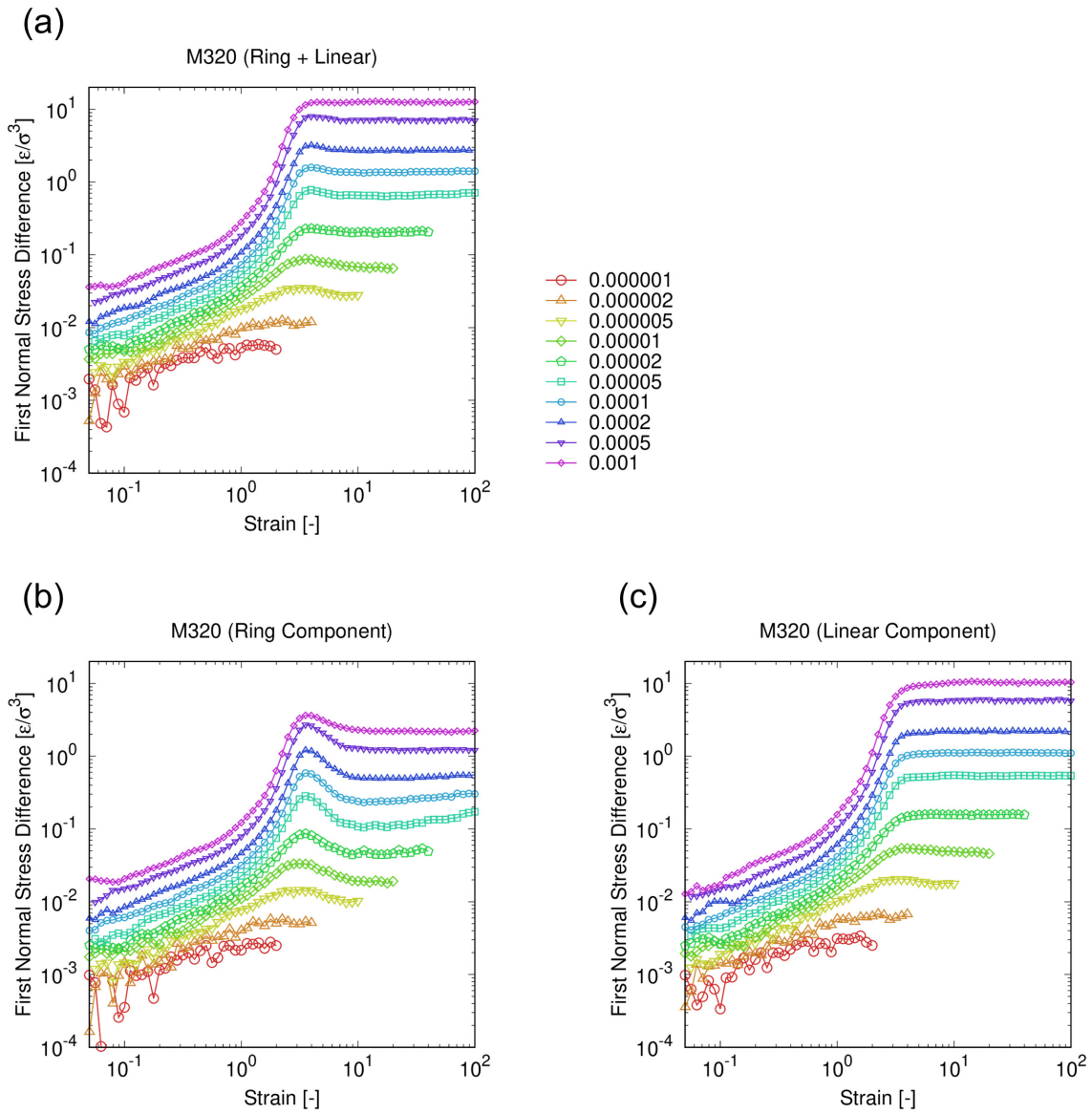


**Figure 4.** Decomposition of the first normal stress difference  $N_1 = \sigma_{zz} - 0.5[\sigma_{xx} + \sigma_{yy}]$  for the M320 blend ( $N = 320, Z = 4$ ) as a function of Hencky strain. (a) Total stress of the ring-linear blend, (b) contribution from the ring component, and (c) contribution from the linear component. The results show that the stress overshoot is primarily driven by the ring component.

This emergence of a stress peak in the ring component is highly dependent on the chain length. The corresponding data for  $N = 80$  and  $160$  are provided in the Supporting Information. As shown in **Figure S2b** for the M160 blend ( $Z = 2$ ), the ring component exhibits only a subtle stress overshoot at the higher strain rates. However, its magnitude is insufficient to induce a clear overshoot in the total stress of the blend (**Figure S2a**), where monotonic growth remains dominant. For the even shorter M80 blend ( $Z = 1$ ), no overshoot is observed in either the ring or the linear component, as shown in **Figure S3**, with both exhibiting purely monotonic stress growth. The comparison between **Figures 4, S2, and S3** highlights that while rings have an inherent tendency to exhibit overshoot when blended with linear chains, a threshold chain length of approximately  $Z \approx 4$  is required for the threading to be sufficiently persistent to produce a macroscopic rheological signature.

To bridge the gap between macroscopic stress behavior and microscopic chain dynamics, we analyzed the conformational changes of the polymer chains during elongational flow. In the following analysis, we focus on the results obtained at a strain rate of  $\dot{\epsilon} = 0.0001$ , as this rate corresponds to the regime where the stress overshoot is prominently observed, allowing for a clear characterization of the structural transitions. **Figure 5** shows snapshots and the probability distributions of the maximum intramolecular distance for the M320 blend at various Hencky strains. Here, the maximum intramolecular distance is defined as the largest separation between any two beads within a single chain, serving as a robust indicator of chain extension; a value close to the contour length signifies a fully stretched, rod-like conformation.

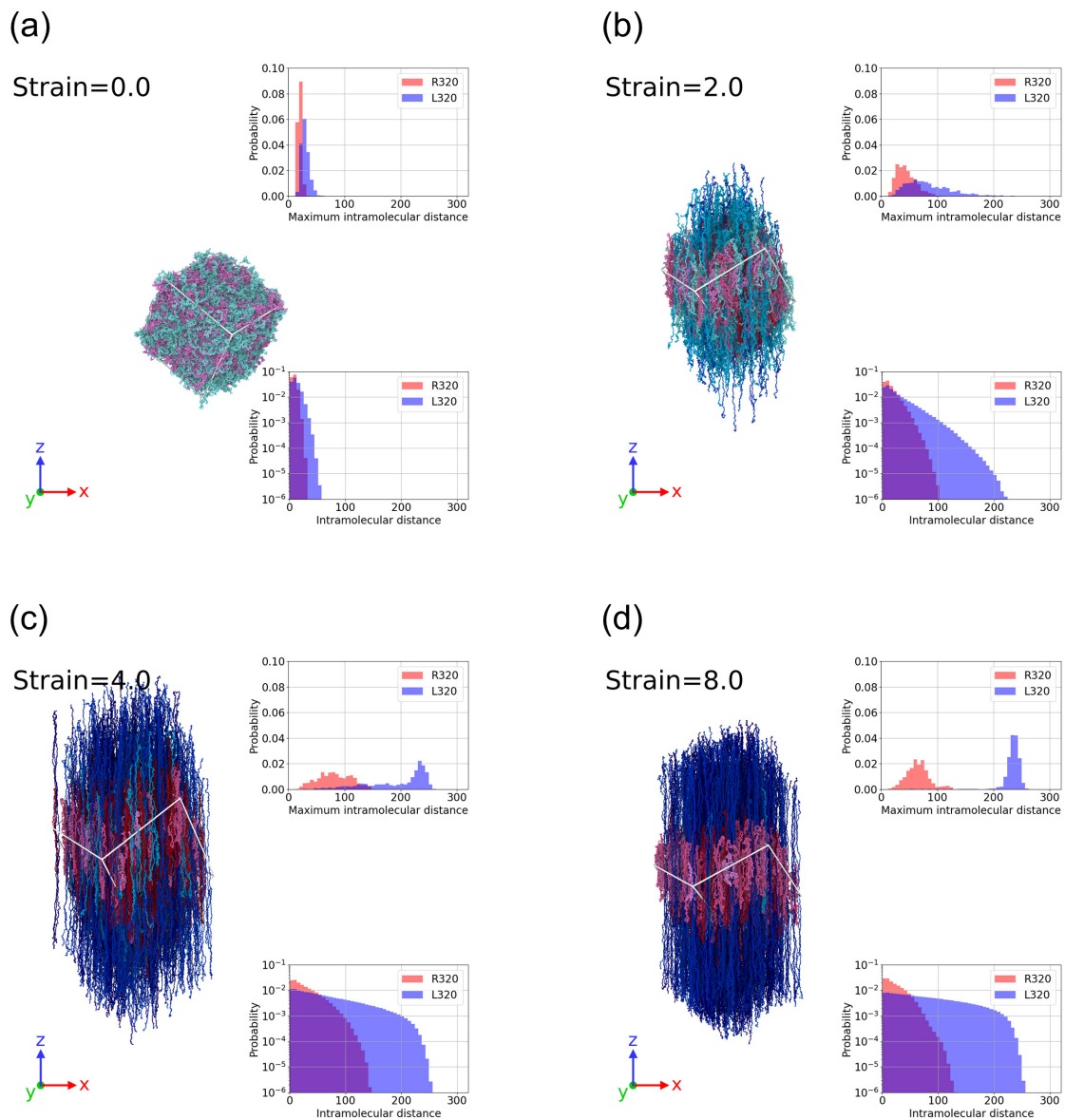


**Figure 5.** Chain conformation analysis and snapshots of the M320 ring-linear blend under  $\epsilon = 0.0001$  at Hencky strains of (a) 0.0, (b) 2.0, (c) 4.0, and (d) 8.0. The white frames correspond to the unit cell shape at each strain. Each chain is unwrapped to maintain its structural continuity and is positioned such that its center of mass resides within the unit cell. In the snapshots, ring and linear polymers are represented in reddish and bluish color scales, respectively. The color intensity of each individual chain was assigned based on its maximum intramolecular distance:

lighter shades correspond to smaller distances, while darker shades indicate larger distances. The accompanying plots show the probability distribution of the maximum intramolecular distance and the individual intramolecular distance for ring (R320) and linear (L320) chains.

In the snapshots, ring and linear polymers are colored in reddish and bluish scales, respectively, with darker shades indicating more highly stretched chains (larger maximum intramolecular distances). At equilibrium (**Figure 5a**, strain of 0.0), both components exhibit coiled conformations with a narrow distribution of intramolecular distances. As the strain increases to 2.0 and 4.0 (**Figures 5b and c**, respectively), the distributions shift significantly toward larger distances, and the snapshots show a clear increase in dark-shaded chains, indicating that both rings and linear chains are being stretched along the elongational direction. Notably, as the stress increases further (strain  $\approx 4$ ), the ring component shows a wide distribution extending to the maximum possible distance, confirming that many rings are in a highly stretched state due to the strong topological constraints imposed by the multiple threading of linear chains. However, at a higher strain of 8.0 (**Figure 5d**), while the linear chains remain in a highly stretched steady state, the distribution for the ring component slightly shifts back toward smaller distances, and the intensity of the dark-red chains decreases. This visual evidence supports the thread-to-unthread transition: after reaching a maximum stretch, the ring polymers contract as the linear chains eventually unthread, resulting in the relaxation of the ring's conformational tension and the subsequent stress overshoot observed in **Figure 4**.

## 4. Discussion

### 4.1. Topological Constraint Analysis via Gauss Linking Number

To provide quantitative evidence for the thread-to-unthread transition, we performed a statistical analysis of the topological constraints using the Gauss linking number. Because the Gauss linking number is strictly defined for a pair of closed loops, we applied a numerical procedure to evaluate the threading between a ring and a linear chain. For each ring and linear chain pair in the system, we artificially closed the linear chain into a loop by extending its two ends in the direction away from the center of mass and connecting them in a large arc.<sup>8</sup> This arc was constructed sufficiently far from the ring to ensure that it did not inadvertently penetrate the ring's surface. In this quasi-ring and ring system, if the original linear chain had threaded through the ring, the resulting pair formed a catenane-like structure with a Gauss linking number of 1.

**Figure 6** shows the probability distribution of the number of penetrations per ring obtained using this method. While the results discussed thus far have been based on a baseline strain rate of  $\dot{\epsilon} = 0.0001$ , we examined the  $N = 80$  (M80) blend at a higher rate of  $\dot{\epsilon} = 0.001$  because the former rate was below the reciprocal of its longest relaxation time ( $1/\tau_d$ ), placing it in the linear viscoelastic regime. To enable a systematic comparison across different chain lengths at identical flow strengths, the results for the  $N = 160$  (M160) blend are presented at both strain rates. This allows for a direct comparison between  $N = 320$  and 160 at  $\dot{\epsilon} = 0.0001$  (**Figures 6a and b**), and between  $N = 160$  and 80 at  $\dot{\epsilon} = 0.001$  (**Figures 6c and d**).

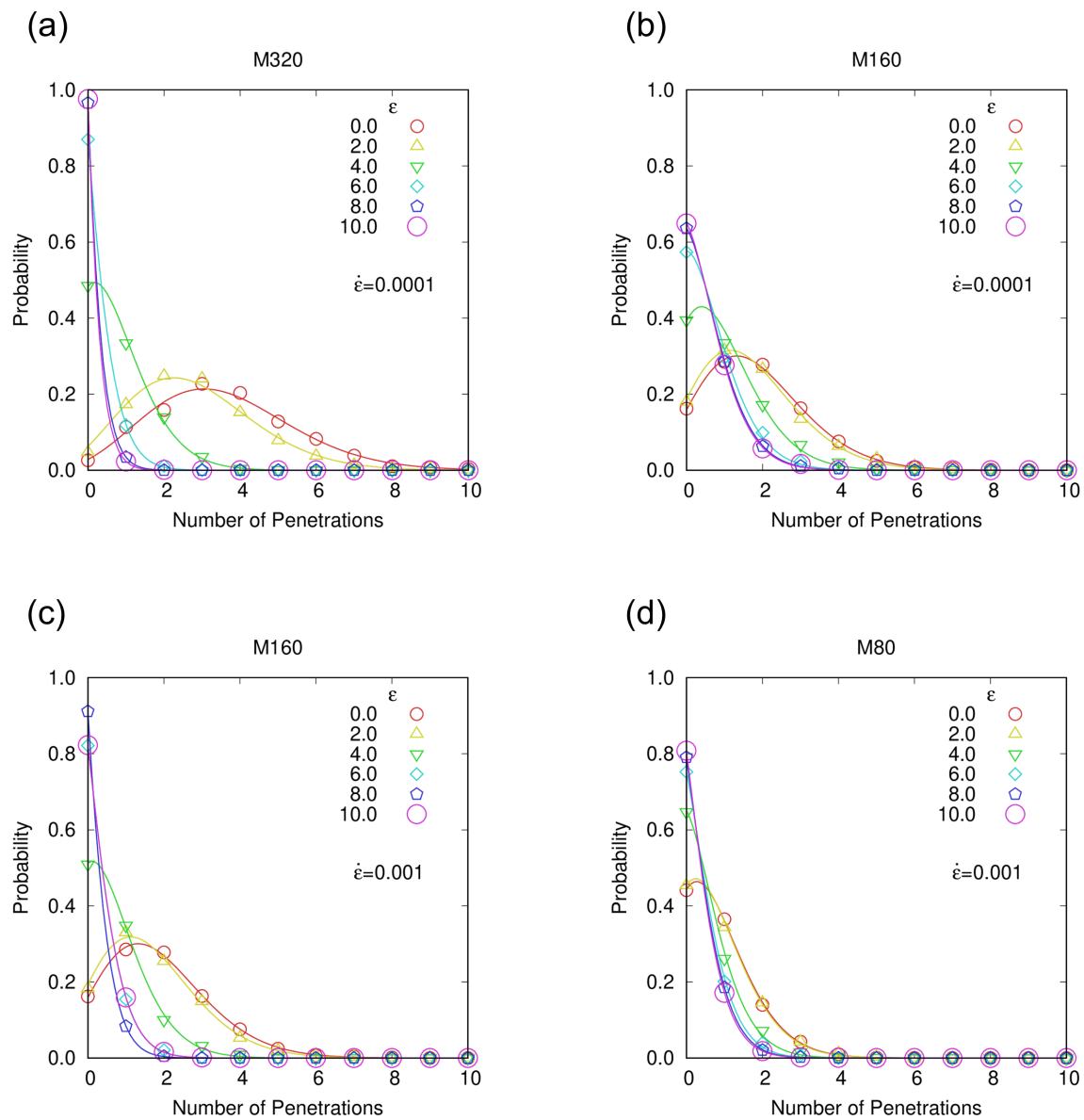


**Figure 6.** Probability distribution of the number of penetrations (threading) per ring for (a) M320 and (b) M160 at a low strain rate ( $\dot{\varepsilon} = 0.0001$ ) and (c) M160 and (d) M80 at a high strain rate ( $\dot{\varepsilon} = 0.001$ ). Threading was evaluated using the Gauss linking number. The results indicate that the number of penetrations decreases as strain increases, triggering the unthreading transition.

For the M320 blend (**Figure 6a**), each ring is penetrated by multiple linear chains at equilibrium (strain of 0.0), with the distribution peaking at approximately three to four penetrations. This confirms the presence of a well-developed threading-mediated entanglement network. As the Hencky strain increases, the distribution shifts significantly toward zero. At a strain of 4.0, which corresponds to the stress peak, the peak of the distribution has already moved to a lower number of penetrations. By a strain of 8.0, the majority of rings have zero penetrations, indicating that most linear chains have unthreaded from the rings. This dramatic reduction in topological constraints directly correlates with the relaxation of the ring component's stress observed in **Figure 4b**. In contrast, for shorter chains such as M160 (**Figures 6b and c**) and M80 (**Figure 6d**), the average number of penetrations at equilibrium is much lower. For M80, most rings have either zero or only one penetration even at equilibrium. The comparison across **Figures 6a–d** suggests that a high initial degree of multiple threading is a necessary condition for sustaining sufficient conformational tension to produce a macroscopic stress overshoot. The rapid release of these multiple constraints during elongational flow is the fundamental molecular mechanism driving the observed non-linear rheological signature in the M320 blend.

## 4.2. Direct Visualization of the Thread-to-Unthread Transition

To provide a more intuitive and microscopic view of the transition mechanism, we monitored the structural evolution of a representative ring-linear complex. **Figure 7** displays a series of snapshots for a specific configuration of the M320 blend, where a single ring (colored in red) is initially threaded by four linear chains (shown in lighter colors). To clarify the dynamics of this specific cluster, the chains were shifted such that their centers of mass remain within the periodic simulation cell throughout the deformation process. At the onset of flow and up to a Hencky

strain of 4.0 (**Figures 7a–c**), the four penetrating linear chains act as temporary topological cross-links. As the linear chains are stretched by the elongational flow, they drag the ring along the flow direction, forcing it into a highly extended, near-rod-like conformation. Specifically, at the strain of 4.0, the ring is threaded by two linear chains that exert frictional forces in opposite directions (along the positive and negative z-axes), effectively stretching the ring open. This state corresponds to the peak of the ring’s stress contribution observed in **Figure 4b**. However, as the strain further increases to 8.0 (**Figure 7d**), the linear chains are observed to eventually unthread or slip out from the ring’s cavity. Once the topological constraints, acting as an internal expansive force on the ring, are released, the ring is no longer supported by the tension of the linear chains and spontaneously contracts to a more relaxed, mildly stretched state. This direct visualization of the thread-to-unthread transition confirms that the macroscopic stress overshoot is not merely a collective effect but is rooted in the dynamic release of multiple threading constraints at the individual chain level.

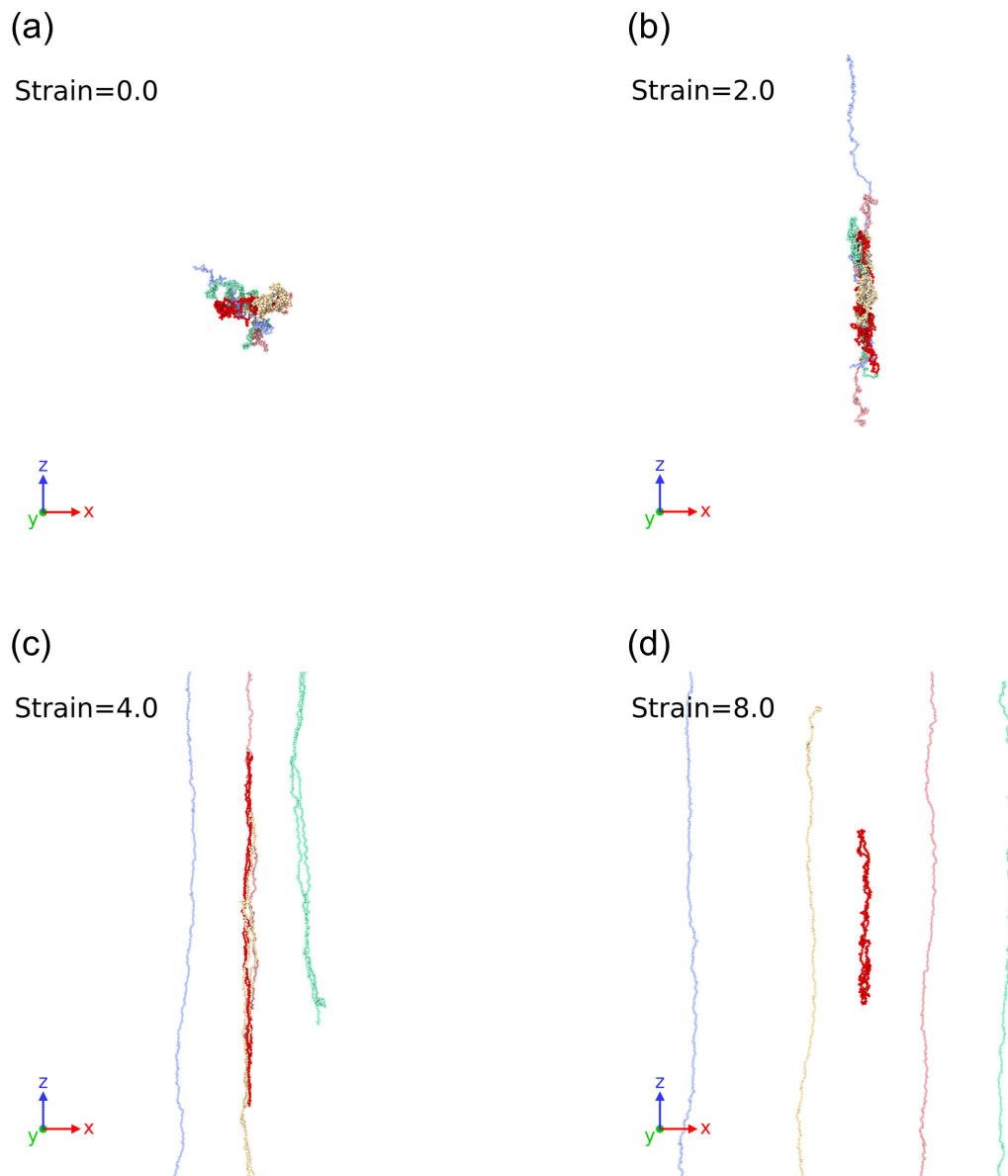


**Figure 7.** Representative visualization of the thread-to-unthread transition under uniaxial elongational flow for the M320 blend at  $\dot{\epsilon} = 0.0001$ . For clarity, a specific configuration where four linear chains penetrate a single ring was selected for visualization. Snapshots at Hencky strains of (a) 0.0, (b) 2.0, (c) 4.0, and (d) 8.0 illustrate the dynamic process: the ring (red) is significantly stretched by the multiple threading of linear chains (light colors) before contracting as the linear chains unthread. To maintain the integrity of the molecular structures, the positions

of the chains were shifted such that their centers of mass remain within the periodic simulation cell.

### 4.3. Real-Space Probability Density Analysis

To further corroborate the ring contraction following the stress overshoot, we evaluated the real-space probability density of the segments for the ring and linear components. To compute these profiles, we first mapped the segment positions onto a three-dimensional grid with a mesh size of  $1\sigma$  using linear interpolation. The density values were calculated by first aligning the center of mass of each chain at the origin and then averaging over all chains of the same species and multiple independent configurations. The resulting probability density is normalized such that its integral over the entire volume equals the total number of segments  $N$  per chain. **Figure 8** shows the density profiles along the elongational direction ( $z$  axis) and the perpendicular directions ( $x$  or  $y$ ) at various Hencky strains for the M320 blend. Because the system maintains symmetry in the  $x$ - $y$  plane perpendicular to the elongational axis, the density profiles in these directions were calculated by taking a cylindrical average around the  $z$  axis to improve statistical accuracy. To provide the further structural details, **Table 2** summarizes the radius of gyration ( $R_g$ ) and its components along  $z$  axis ( $R_{g,z}$ ) and perpendicular direction ( $R_{g,\perp} = \sqrt{R_{g,x}^2 + R_{g,y}^2}$ ) for both rings and linear chains in the M320 blend.

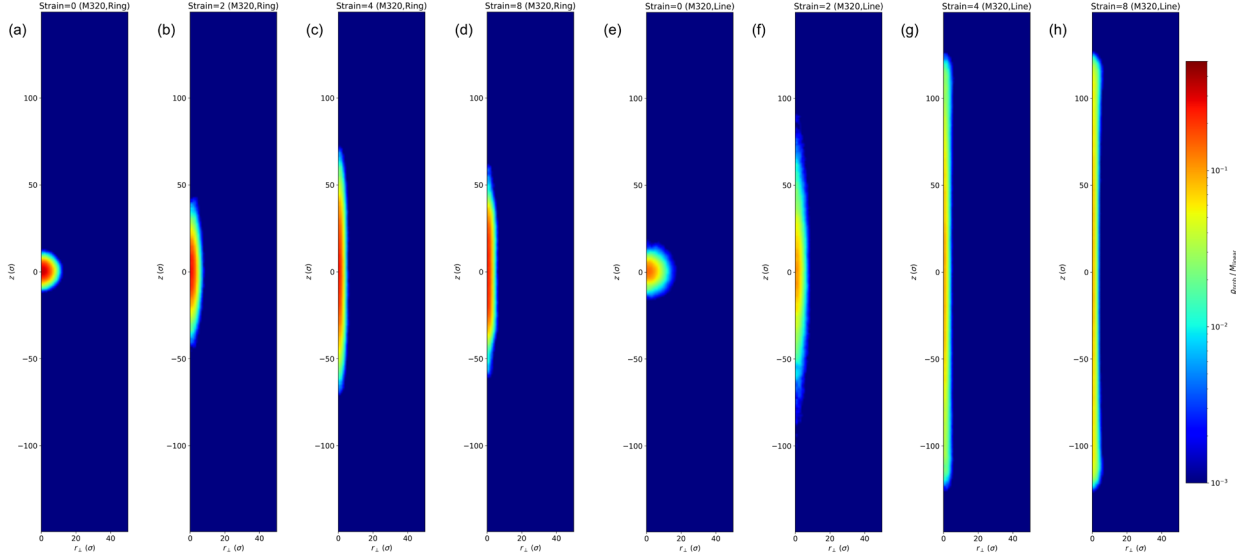


**Figure 8.** Real-space probability density of ring and linear components in the M320 blend ( $\epsilon = 0.0001$ ) at Hencky strains of (a) 0.0, (b) 2.0, (c) 4.0, and (d) 8.0 for ring components, and (e) 0.0, (f) 2.0, (g) 4.0, and (h) 8.0 for linear components. Here,  $r_{\perp} = \sqrt{x^2 + y^2}$ .

**Table 2.** Radius of gyration ( $R_g$ ) and its components along  $z$  axis ( $R_{g,z}$ ) and perpendicular direction ( $R_{g,\perp} = \sqrt{R_{g,x}^2 + R_{g,y}^2}$ ) for rings and linear chains in the M320 blend. Note that  $R_g^2 = R_{g,z}^2 + 2R_{g,\perp}^2$ .

	Topology	Strain = 0	Strain = 2	Strain = 4	Strain = 8
$R_g$	Ring	$6.3\sigma$	$13.1\sigma$	$24.5\sigma$	$19.9\sigma$
	Linear	$9.4\sigma$	$25.7\sigma$	$59.8\sigma$	$71.6\sigma$
$R_{g,z}$	Ring	$3.5\sigma$	$12.6\sigma$	$24.3\sigma$	$19.7\sigma$
	Linear	$5.1\sigma$	$25.3\sigma$	$59.7\sigma$	$71.6\sigma$
$R_{g,\perp}$	Ring	$3.6\sigma$	$2.3\sigma$	$1.6\sigma$	$1.7\sigma$
	Linear	$5.3\sigma$	$2.8\sigma$	$1.7\sigma$	$1.6\sigma$

Consistent with the conformational analysis of **Figure 5**, the ring component exhibits a dramatic expansion and subsequent contraction in real space. At the stress peak (strain of 4.0), the probability density of the ring segments shows its broadest distribution along the  $z$  axis, indicating that the rings are stretched to their maximum spatial extent along the elongational direction. However, as the strain increases to 8.0, the distribution width of the ring component along the  $z$  axis decreases, accompanied by an increase in the peak density at the center. This spatial contraction serves as a direct structural signature of the unthreading process, where the release of multiple topological constraints allows the ring to recoil despite the continuous elongational flow. In contrast, the linear component displays a different trend. As shown in the corresponding density profiles, the linear chains reach a maximum degree of extension by  $\epsilon = 8.0$ . This lack of contraction in the linear component reinforces our conclusion that the stress overshoot is a phenomenon unique to the ring polymers in the blend, driven by the dynamic transition from a threaded, highly stretched state to an unthreaded, relaxed state.

At a strain rate of  $\dot{\epsilon} = 0.0001$ , which is sufficiently fast compared to the reciprocal of the longest relaxation times of both rings and linear chains, both components reach a highly stretched steady state. In this steady state, the average extension of each chain is generally determined by the balance between the outward drag force from the elongational flow and the inward entropic tension of the chain itself. However, the presence of the stress overshoot in the ring component suggests that there is an additional mechanism at play. The microscopic origin of the overshoot lies in the “extra stretching” of the ring polymers. During the initial stages of deformation, the linear chains that penetrate the ring act as moving constraints that actively pull the ring along the flow direction. This coupling generates a transient extension that exceeds the degree of stretching by flow-drag alone. As the linear chains eventually unthread, this extra

pulling force vanishes, and the ring contracts to its steady-state length where only the flow-drag and entropic tension are balanced. This structural transition is clearly captured in **Figures 8c and d**, where the  $z$  axis distribution of the ring component at  $\epsilon = 4.0$  (the stress peak) is broader than at  $\epsilon = 8.0$  (the steady state).

#### 4.4. Predicted SANS Patterns for Experimental Validation

Finally, we propose an experimental approach to validate the thread-to-unthread transition using SANS. As suggested by **Figure 8**, the average conformation of the rings is expected to be strain dependent. There is a strong motivation to capture this transition through direct experimental observation; indeed, SANS measurements on labeled rings<sup>11,12,51-54</sup> have already proven to be a viable method for this purpose. In a previous experimental study, Borger et al.<sup>20</sup> utilized SANS to investigate the same phenomenon. Specifically, they employed a labeling strategy in which 10% of deuterated linear chains were incorporated as tracers to monitor the conformational changes of the linear component. By comparing the scattering profiles of the ring-linear blend with those of a pure linear melt, they aimed to isolate the effects of the ring-linear topological interactions. This experimental design was strategically chosen to detect how the presence of rings induces extra stretching in the ring-linear entanglement network. Measuring the ring component directly under flow remains experimentally challenging. In particular, isolating the scattering contribution of the ring component by substituting 10% of the rings with their deuterated counterparts is a significant challenge. While some specialized studies have successfully employed deuterated rings for SANS measurements<sup>11,12,51-54</sup>, the prohibitive cost and the synthetic difficulty of ensuring the absence of linear contaminants when scaling up production to the levels required for precise structural analysis under flow have largely restricted

more widespread validation. Our simulation, free from such contrast constraints, provides a complementary perspective by predicting the structural evolution of the ring component itself. While Borger et al.<sup>20</sup> provided indirect evidence of the transition through the deformation of the linear matrix, our results offer a more direct structural signature: the post-peak relaxation of ring anisotropy.

The predicted scattering intensity  $I(\mathbf{q})$  was calculated based on the total coherent scattering from the  $N$  segments of each chain as  $I(\mathbf{q}) = \left\langle \left| \sum_{j=1}^N \exp(i\mathbf{q} \cdot \mathbf{r}_j) \right|^2 \right\rangle$ , where  $\mathbf{q}$  is the wave vector and  $\mathbf{r}_j$  is the position of the  $j$ -th segment. Here, the angular brackets  $\langle \dots \rangle$  denote the ensemble average over all chains of the same topology (i.e., either linear or ring). This definition ensures that the scattering intensity properly reflects the overall size and shape of the molecules, with  $I(0) = N^2$  in the limit of small  $q$ . To improve statistical accuracy and account for the symmetry of the uniaxial elongational flow, the 2D SANS patterns in the  $q_z$ - $q_\perp$  plane were obtained by performing a cylindrical average in  $q$ -space ( $q_\perp = \sqrt{q_x^2 + q_y^2}$ ), consistent with the real-space probability density analysis. **Figure 9** shows the predicted 2D SANS patterns for the M320 blend.

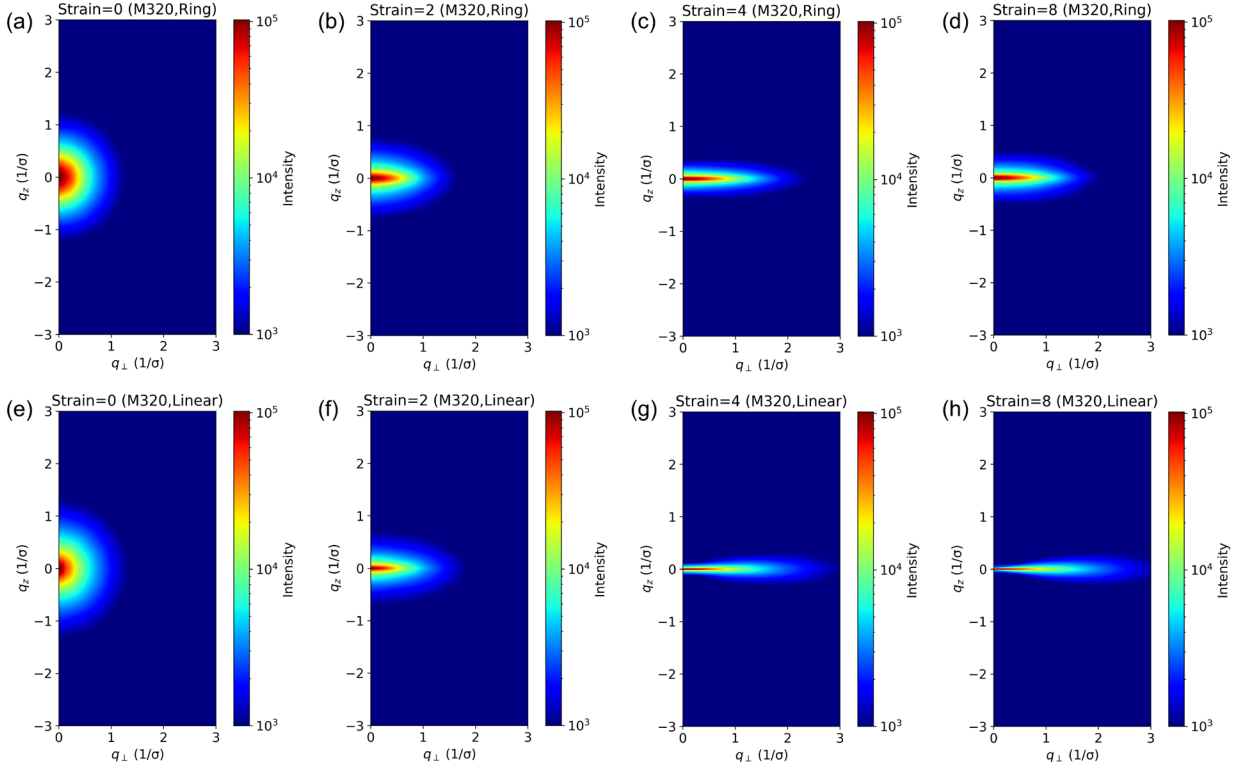


**Figure 9.** Predicted 2D SANS patterns for experimental validation of the unthreading mechanism. Patterns (a–d) correspond to the ring component and (e–h) to the linear component in the M320 blend ( $\dot{\epsilon} = 0.0001$ ) at various strains. The ring component shows maximum anisotropy at the stress peak ( $\epsilon = 4.0$ ) and a shift toward a more relaxed state at  $\epsilon = 8.0$  due to unthreading.

For the ring component (**Figures 9a–d**), the scattering pattern exhibits a dramatic evolution that corresponds to the stress overshoot. As the strain increases, the scattering intensity becomes increasingly localized near  $q_z = 0$  while simultaneously extending toward the high- $q_{\perp}$  region. Notably, at the stress peak ( $\epsilon = 4.0$ ), this anisotropy reaches its maximum, where the intensity is highly localized near  $q_z = 0$ . This narrow width in  $q_z$  reflects the maximally extended, rod-like conformation of the rings held by multiple threading constraints as shown in **Figure 7**. Beyond

the stress peak, as the rings become unthreaded, the scattering intensity starts to spread along the  $q_z$  direction, signaling the onset of structural relaxation. By  $\epsilon = 8.0$ , the distribution in  $q_z$  becomes notably broader than at  $\epsilon = 4.0$ , which is consistent with the spatial contraction of the rings observed in **Figures 8c–d**. This shift from a high anisotropic state to a more relaxed state following the stress peak serves as a structural signature of the unthreading process.

In contrast, the linear component (**Figures 9e–h**) maintains a highly anisotropic pattern from  $\epsilon = 4.0$  to  $8.0$ , reflecting its steady-state extension. Specifically, the scattering intensity is sharply concentrated at  $q_z \approx 0$  in the low- $q_\perp$  region, indicating a significant increase in the correlation length along the  $z$  axis as the chains extend and align with the stretching direction. Meanwhile, the pattern exhibits a broader distribution along the  $q_z$  direction at higher  $q_\perp$ , which can be attributed to local segmental fluctuations that deviate from the perfectly oriented backbone.

To further investigate the structural anisotropy, 1D intensity profiles were extracted from the 2D-SANS patterns along the  $q_z$  and  $q_\perp$  axes shown in **Figure S4** in the Supporting Information. Guinier analysis of these 1D profiles (**Figure S5**) yielded the radius of gyration components,  $R_{g,z}$  and  $R_{g,\perp}$  which are summarized in **Table S1**. These values were found to be in good agreement with the values calculated directly from the coordinate data presented in **Table 2**, confirming the validity of our analysis.

The successful detection of these distinct 2D SANS signatures, especially the post-peak relaxation of the ring anisotropy, would provide definitive experimental evidence for the threshold chain length and the multiple threading mechanism identified in this study. In this context, our identification of the threshold chain length at  $Z \approx 4$  is of significant practical importance for experimentalists. Previous reports of stress overshoot in ring-linear blends utilized systems with  $Z \approx 14$ ,<sup>17,20</sup> which require the synthesis of high-molar mass ring

polymers—a task that is difficult to achieve while maintaining high topological purity. By demonstrating that the multiple threading mechanism and the resulting stress overshoot manifest at a much lower threshold ( $Z \approx 4$ ), our work suggests that the experimental hurdle for direct structural validation is considerably lower than previously assumed. This means that researchers can focus on moderately entangled systems, for which the synthesis and LCCC purification of rings are more accessible. While reducing  $Z$  eases the chemical challenges, it inherently shifts the experimental requirement toward faster deformation rates. Researchers must therefore balance the accessibility of purified rings with the technical limits of extensional rheometry, as shorter chains require significantly higher strain rates.

Nevertheless, the primary remaining challenge lies in the sophisticated material preparation required for definitive SANS characterization, specifically the synthesis of topologically pure deuterated ring polymers at sufficient quantities and purity levels for structural analysis. While pioneering SANS experiments on ring polymers<sup>11,12,50–53</sup> have already been reported, the synthetic constraints associated with long chains have limited the scope of direct structural validation. We hope that the lower chain length requirement identified here, combined with future breakthroughs in polymer chemistry, will soon enable the direct validation of the molecular recoil and unthreading dynamics predicted in this study.

## 5. Summary

In this study, we investigated the chain-length dependence of the uniaxial elongational rheology of equi-weight ring-linear polymer blends using coarse-grained molecular dynamics simulations. Our systematic analysis revealed a clear topological origin for the stress-overshoot

phenomena, providing a unified understanding of the role of threading across different entanglement regimes. The main findings of this work are as follows:

*Identification of the Threshold Chain Length:* We identified that a threshold chain length of  $Z \approx 4$  ( $N = 320$ ) is required for the emergence of a macroscopic stress overshoot in ring-linear blends under uniaxial elongational flow. Blends with shorter chains ( $Z \leq 2$ ) exhibit monotonic stress growth even under high strain-rate flow conditions.

*Role of Multiple Threading:* Our topological analysis using the Gauss linking number revealed that at the identified threshold ( $Z \approx 4$ ), each ring is penetrated by multiple linear chains (averaging three to four) at equilibrium. These multiple threading events are essential to provide a sufficiently strong topological grip, allowing the rings to be stretched significantly alongside the linear entanglement network.

*Molecular Mechanism of Overshoot:* The stress overshoot is quantitatively linked to a transient thread-to-unthread transition. Stress decomposition and conformational analysis confirmed that the peak stress corresponds to the maximum extension of the rings, followed by a stress drop as the linear chains unthread, leading to the structural recoil of the ring component.

*Structural Evolution via 2D Scattering Patterns:* We demonstrated that the 2D scattering patterns of the single ring component exhibit a distinct evolution that reflects the macroscopic stress response. As the rings reach their maximum extension at the stress peak, the scattering intensity becomes sharply concentrated at  $q_z \approx 0$  and expanded along the axis perpendicular to the elongation direction ( $q_{\perp}$ ). Subsequently, this intense anisotropy diminishes as the rings undergo structural recoil during the unthreading process, providing a direct experimental signature for validating the predicted molecular recoil and unthreading dynamics.

Looking forward, our finding that the stress overshoot manifests at a relatively low entanglement number ( $Z \approx 4$ ) provides an important guideline for future experimental validations. While previous studies<sup>17,20</sup> focused on high-molar mass systems ( $Z \approx 14$ ), which are notoriously difficult to synthesize and purify, our results suggest that moderately entangled systems are sufficient to capture the physics of the thread-to-unthread transition. Indeed, comprehensive SANS (and neutron spin echo) investigations by Kruteva et al.<sup>11,12</sup> have already established that the fundamental conformational and dynamic signatures of ring-linear topological interactions—such as threading-induced swelling and local relaxation modes—are clearly detectable in pure and blended systems. However, the high synthetic effort required to produce high-purity deuterated rings at very large  $Z$  has limited the exploration of non-linear structural evolution under fast flows. In the moderately entangled regime ( $Z \approx 4$ ), the preparation of topologically pure samples via LCCC is more accessible. We hope that the predicted 2D SANS patterns for  $Z \approx 4$  systems will encourage experimentalists to utilize moderately entangled, deuterated ring polymers to directly observe the molecular recoil and unthreading dynamics predicted in this study.

## ASSOCIATED CONTENT

### **Supporting Information.**

The following file is available free of charge.

SupportingInformation.pdf (PDF)

Stress overshoot behavior under uniaxial elongational flow at a longer chain system; rheological decomposition of shorter chain blends; 1D SANS profiles and Guinier plots.

## AUTHOR INFORMATION

### **Corresponding Author**

**Takahiro Murashima** – Department of Physics, Tohoku University, 6-3, Aramaki-aza-Aoba, Aoba-ku, Sendai, 980-8578, Japan; Email: [murasima@cmpt.phys.tohoku.ac.jp](mailto:murasima@cmpt.phys.tohoku.ac.jp)

### **Authors**

**Katsumi Hagita** – Department of Applied Physics, National Defense Academy, 1-10-20 Hashirimizu, Yokosuka, 239-8686, Japan.

**Toshihiro Kawakatsu** – Department of Physics, Tohoku University, 6-3, Aramaki-aza-Aoba, Aoba-ku, Sendai, 980-8578, Japan.

### **Author Contributions**

T.M. led the study, performed the coarse-grained molecular dynamics simulations, conducted the data analysis, and developed the physical interpretations. K.H. and T.K. provided technical support and participated in the discussion of the results. All authors have reviewed and approved the final version of the manuscript

### **Funding Sources**

This work was partly financially supported by JSPS KAKENHI, Japan (grant Nos. JP18H04494, JP19H00905, JP20K03875, JP20H04649, JP21H00111, JP25K01839, and JP25K07238), JST CREST, Japan, (JPMJCR1993, JPMJCR19T4, and JPMJCR25Q3), and the Fuji Seal Foundation (T.M.).

## ACKNOWLEDGMENT

T.M. thanks Prof. T. Taniguchi, Prof. M. Sugimoto, Prof. J.-I. Takimoto, Prof. S. K. Sukumaran, Prof. T. Uneyama, Prof. Y. Masubuchi, Prof. Y. Doi, Dr. T. Honda, Dr. Y. Tomiyoshi, Dr. T. Sato, and Dr. N. Sakata for their fruitful discussions, comments, and encouragement. The authors thank Prof. H. Jinnai, Prof. T. Satoh, Prof. T. Deguchi, and Prof. K. Shimokawa for their support and encouragement. T.M. and T.K. thank the collaboration program of the Advanced Imaging and Modeling Center for Soft-materials (AIMcS) of Tohoku University. For the computations in this work, the authors were partially supported by the Supercomputer Center, Institute for Solid State Physics, University of Tokyo; MASAMUNE-IMR at the Center for Computational Materials Science, Institute for Materials Research, Tohoku University; Grand Chariot, Grand Chariot 2, and Polaire at the Hokkaido University Information Initiative Center; Flow at Nagoya University Information Technology Center; SQUID at Cybermedia Center, Osaka University; Genkai at Research Institute for Information Technology, Kyushu University; Miyabi at Information Technology Center, University of Tokyo; Fugaku at RIKEN Center for Computational Science; the Joint Usage/Research Center for Interdisciplinary Large-Scale Information Infrastructures (JHPCN); and the High-Performance Computing Infrastructure (HPCI) in Japan (hp200048, hp200168, hp210102, hp210132, hp220019, hp220104, hp220113, hp220114, hp230384, hp240469, hp250329, hp250144, jh210035, jh220038, jh230026, and jh250040). This work was partly financially supported by JSPS KAKENHI, Japan (grant Nos. JP18H04494, JP19H00905, JP20K03875, JP20H04649, JP21H00111, JP25K01839, and JP25K07238), JST CREST, Japan, (JPMJCR1993, JPMJCR19T4, and JPMJCR25Q3), and the Fuji Seal Foundation (T.M.). The authors thank Editage ([www.editage.com](http://www.editage.com)) for the English language editing.

## REFERENCES

- (1) McLeish, T. Polymer without beginning or end. *Science* **2002**, *297*(5589), 2005–2006. DOI: [10.1126/science.1076810](https://doi.org/10.1126/science.1076810).
- (2) Kapnistos, M.; Lang, M.; Vlassopoulos, D.; Pyckhout-Hintzen, W.; Richter, D.; Cho, D.; Chang, T.; Rubinstein, M. Unexpected power-law stress relaxation of entangled ring polymers. *Nature Materials* **2008**, *7*(12), 997–1002. DOI: [10.1038/nmat2292](https://doi.org/10.1038/nmat2292).
- (3) Doi, M.; Edwards, S. F. *The Theory of Polymer Dynamics*, Clarendon Press, Oxford, 1986.
- (4) Pasch, H.; Trathnigg B. *HPLC of Polymers*, Springer, Berlin, 1997. DOI: [10.1007/978-3-642-58265-3](https://doi.org/10.1007/978-3-642-58265-3).
- (5) Subramanian, G.; Shanbhag, S. Self-diffusion in binary blends of cyclic and linear polymers. *Macromolecules* **2008**, *41*(19) 7239–7242. DOI: [10.1021/ma801232j](https://doi.org/10.1021/ma801232j).
- (6) Jeong, C.; Douglas, J. F. Relation between polymer conformational structure and dynamics in linear and ring polyethylene blends. *Macromolecular Theory and Simulations* **2017**, *26*(5), 1700045. DOI: [10.1002/mats.201700045](https://doi.org/10.1002/mats.201700045).
- (7) Tsalikis, D. G.; Mavrantzas, V. Size and diffusivity of polymer rings in linear polymer matrices: The key role of threading events. *Macromolecules* **2020**, *53*(3) 803–820. DOI: [10.1021/acs.macromol.9b02099](https://doi.org/10.1021/acs.macromol.9b02099).
- (8) Hagita, K.; Murashima, T. Effect of chain-penetration on ring shape for mixtures of rings and linear polymers. *Polymer* **2021**, *218*, 123493. DOI: [10.1016/j.polymer.2021.123493](https://doi.org/10.1016/j.polymer.2021.123493).

- (9) Hagita, K.; Murashima, T. Molecular Dynamics Simulations of Ring Shapes on a Ring Fraction in Ring–Linear Polymer Blends. *Macromolecules* **2021**, *54*(17), 8043–8051. DOI: [10.1021/acs.macromol.1c00656](https://doi.org/10.1021/acs.macromol.1c00656)
- (10) Mo, J.; Wang, J.; Wang, Z.; Lu, Y.; An, L. Size and dynamics of a tracer ring polymer embedded in a linear polymer chain melt matrix. *Macromolecules* **2022**, *55*(5) 1505–1514. DOI: [10.1021/acs.macromol.1c02388](https://doi.org/10.1021/acs.macromol.1c02388).
- (11) Kruteva M.; Allgaier J.; Richte D. Topology matters: Conformation and microscopic dynamics of ring polymers. *Macromolecules* **2023**, *56*(18),7203 – 7229. DOI: [10.1021/acs.macromol.3c00560](https://doi.org/10.1021/acs.macromol.3c00560).
- (12) Kruteva, M.; Allgaier, J.; Monkenbusch, M.; Falus, P.; Peponaki, K.; Vlassopoulos, D.; Richter D. Dynamics of polymer rings in ring-linear blends by neutron spin echo spectroscopy. *ACS Macro Letters* **2025**, *14*(10), 1396–1401. DOI: [10.1021/acsmacrolett.5c00507](https://doi.org/10.1021/acsmacrolett.5c00507)
- (13) Roovers, J. Viscoelastic properties of polybutadiene rings. *Macromolecules* **1988**, *21*(5), 1517–1521. DOI: [10.1021/ma00183a049](https://doi.org/10.1021/ma00183a049).
- (14) Halverson, J. D.; Grest, G. S.; Grosberg, A. Y.; Kremer, K. Rheology of ring polymer melts: from linear contaminants to ring-linear blends. *Physical Review Letters* **2012**, *108*(3), 038301. DOI: [10.1103/PhysRevLett.108.038301](https://doi.org/10.1103/PhysRevLett.108.038301).
- (15) Parisi, D.; Ahn, J.; Chang, T.; Vlassopoulos, D.; Rubinstein, M. Stress relaxation in symmetric ring/linear polymer blends at low ring fractions. *Macromolecules* **2020**, *53*(5), 1685–1693. DOI: [10.1021/acs.macromol.9b02536](https://doi.org/10.1021/acs.macromol.9b02536).

- (16) Tomiyoshi, Y.; Murashima, T.; Kawakatsu, T. Single-chain slip-spring simulation for entangled ring/linear polymer blends at low ring fractions. *Macromolecules* **2023**, *56*(23), 9896–9904. DOI: [10.1021/acs.macromol.3c01454](https://doi.org/10.1021/acs.macromol.3c01454).
- (17) O'Connor, T. C.; Ge, T.; Grest, G. S. Composite entanglement topology and extensional rheology of symmetric ring-linear polymer blends. *Journal of Rheology* **2022**, *66*(1), 49–65. DOI: [10.1122/8.0000319](https://doi.org/10.1122/8.0000319).
- (18) Zhou, Y.; Hsiao, K.-W.; Regan, K. E.; Kong, D.; McKenna, G. B.; Robertson-Anderson, R. M.; Schroeder, C. M. Effect of molecular architecture on ring polymer dynamics in semidilute linear polymer solutions. *Nature Communications* **2019**, *10*(1), 1753. DOI: [10.1038/s41467-019-09627-7](https://doi.org/10.1038/s41467-019-09627-7).
- (19) Zhou, Y.; Young, C. D.; Lee, M.; Banik, S.; Kong, D.; McKenna, G. B.; Robertson-Anderson, R. M.; Sing, C. E.; Schroeder, C. M. Dynamics and rheology of ring-linear blend semidilute solutions in extensional flow: single molecule experiments. *Journal of Rheology* **2021**, *65*(4), 729–744. DOI: [10.1122/8.0000219](https://doi.org/10.1122/8.0000219).
- (20) Borger, A.; Wang, W.; O'Connor, T. C.; Ge, T.; Grest, G. S.; Jensen, G. V.; Ahn, J.; Chang, T.; Hassager, O.; Mortensen, K.; Vlassopoulos, D.; Huang, Q. Threading–unthreading transition of linear-ring polymer blends in extensional flow. *ACS Macro Letters* **2020**, *9*(10), 1452–1457. DOI: [10.1021/acsmacrolett.0c00607](https://doi.org/10.1021/acsmacrolett.0c00607).
- (21) Murashima, T.; Hagita, K.; Kawakatsu, T. Viscosity overshoot in biaxial elongational flow: coarse-grained Molecular Dynamics simulation of ring-linear polymer mixtures. *Macromolecules* **2021**, *54*(15), 7210–7225. DOI: [10.1021/acs.macromol.1c00267](https://doi.org/10.1021/acs.macromol.1c00267).

- (22) Kremer, K.; Grest, G. S. Dynamics of entangled linear polymer melts: A molecular-dynamics simulation. *Journal of Chemical Physics* **1990**, *92*(8), 5057–5086. DOI: [10.1063/1.458541](https://doi.org/10.1063/1.458541).
- (23) Everaers, R.; Sukumaran, S. K.; Grest, G. S.; Svaneborg, C.; Sivasubramanian, A.; Kremer, K. Rheology and microscopic topology of entangled polymeric liquids. *Science* **2004**, *303*(5659), 823–826. DOI: [10.1126/science.1091215](https://doi.org/10.1126/science.1091215).
- (24) Sukumaran, S. K.; Grest, G. S.; Kremer, K.; Everaers, R. Identifying the Primitive Path Mesh in Entangled Polymer Liquids. *Journal of Polymer Science Part B: Polymer Physics* **2005**, *43*(8), 917–933. DOI: [10.1002/polb.20384](https://doi.org/10.1002/polb.20384).
- (25) Kröger, M. Shortest multiple disconnected path for the analysis of entanglements in two- and three-dimensional polymeric systems. *Computer Physics Communications* **2005**, *168*(3), 209–232. DOI: [10.1016/j.cpc.2005.01.020](https://doi.org/10.1016/j.cpc.2005.01.020).
- (26) Tzoumanekas, C.; Theodorou, D. N. Topological Analysis of Linear Polymer Melts: A Statistical Approach. *Macromolecules* **2006**, *39*(13), 4592–4604. DOI: [10.1021/ma0607057](https://doi.org/10.1021/ma0607057).
- (27) Hoy, R. S.; Foteinopoulou, K.; Kröger, M. Topological analysis of polymeric melts: chain-length effects and fast-converging estimators for entanglement length. *Physical Review. E, Statistical, Nonlinear, and Soft Matter Physics* **2009**, *80*(3), 031803. DOI: [10.1103/PhysRevE.80.031803](https://doi.org/10.1103/PhysRevE.80.031803).
- (28) Svaneborg, C.; Everaers, R. Characteristic Time and Length Scales in Melts of Kremer-Grest Bead-Spring Polymers with Wormlike Bending Stiffness. *Macromolecules* **2020**, *53*(6), 1917–1941. DOI: [10.1021/acs.macromol.9b02437](https://doi.org/10.1021/acs.macromol.9b02437).

- (29) Dietz, J. D.; Kröger, M.; Hoy, R. S. Validation and Refinement of Unified Analytic Model for Flexible and Semiflexible Polymer Melt Entanglement. *Macromolecules* **2022**, *55*(9), 3613–3626. DOI: [10.1021/acs.macromol.1c02597](https://doi.org/10.1021/acs.macromol.1c02597).
- (30) Kröger, M.; Dietz, J. D.; Hoy, R. S.; Luap, C. The Z1+ package: Shortest multiple disconnected path for the analysis of entanglements in macromolecular systems. *Computer Physics Communications* **2023**, *283*, 108567. DOI: [10.1016/j.cpc.2022.108567](https://doi.org/10.1016/j.cpc.2022.108567)
- (31) Dobson, M. Periodic boundary conditions for long-time nonequilibrium Molecular Dynamics simulations of incompressible flows. *Journal of Chemical Physics* **2014**, *141*(18), 184103. DOI: [10.1063/1.4901276](https://doi.org/10.1063/1.4901276).
- (32) Hunt, T. A. Periodic boundary conditions for the simulation of uniaxial extensional flow of arbitrary duration. *Molecular Simulation* **2015**, *42*(5), 347–352. DOI: [10.1080/08927022.2015.1051043](https://doi.org/10.1080/08927022.2015.1051043).
- (33) Nicholson, D. A.; Rutledge, G. C. Molecular simulation of flow-enhanced nucleation in N-Eicosane melts under steady shear and uniaxial extension. *Journal of Chemical Physics* **2016**, *145*(24), 244903. DOI: [10.1063/1.4972894](https://doi.org/10.1063/1.4972894).
- (34) O'Connor, T. C.; Alvarez, N. J.; Robbins, M. O. Relating chain conformations to extensional stress in entangled polymer melts. *Physical Review Letters* **2018**, *121*(4), 047801. DOI: [10.1103/PhysRevLett.121.047801](https://doi.org/10.1103/PhysRevLett.121.047801).
- (35) Murashima, T.; Hagita, K.; Kawakatsu, T. Elongational viscosity of weakly entangled polymer melt via coarse-grained Molecular Dynamics simulation. *Nihon Reoroji Gakkaishi* **2018**, *46*(5), 207–220. DOI: [10.1678/rheology.46.207](https://doi.org/10.1678/rheology.46.207). <https://github.com/t-murash/LAMMPS-UEFEX>.

- (36) Evans, D. J.; Morriss, G. *Statistical Mechanics of Nonequilibrium Liquids*, 2nd ed., Cambridge University Press, 2008. DOI: [10.1017/CBO9780511535307](https://doi.org/10.1017/CBO9780511535307).
- (37) Kraynik, A. M.; Reinelt, D. A. Extensional motions of spatially periodic lattices. *International Journal of Multiphase Flow* **1992**, *18*(6), 1045–1059. DOI: [10.1016/0301-9322\(92\)90074-Q](https://doi.org/10.1016/0301-9322(92)90074-Q).
- (38) Baranyai, A.; Cummings, P. T. Steady state simulation of planar elongation flow by nonequilibrium Molecular Dynamics. *Journal of Chemical Physics* **1999**, *110*(1), 42–45. DOI: [10.1063/1.478082](https://doi.org/10.1063/1.478082).
- (39) Matin, M. L.; Daivis, P. J.; Todd, B. D. Comparison of planar shear flow and planar elongational flow for systems of small molecules. *Journal of Chemical Physics* **2000**, *113*(20), 9122–9131. DOI: [10.1063/1.1319379](https://doi.org/10.1063/1.1319379).
- (40) Anderson, J. A.; Glaser, J.; Glotzer, S. C. HOOMD-blue: A python package for high-performance Molecular Dynamics and hard particle Monte Carlo simulations. *Computational Materials Science* **2020**, *173*, 109363. DOI: [10.1016/j.commatsci.2019.109363](https://doi.org/10.1016/j.commatsci.2019.109363). <http://glotzerlab.engin.umich.edu/hoomd-blue/>.
- (41) Plimpton, S. Fast parallel algorithms for short-range Molecular Dynamics. *Journal of Computational Physics* **1995**, *117*(1), 1–19. DOI: [10.1006/jcph.1995.1039](https://doi.org/10.1006/jcph.1995.1039). <https://lammmps.org/>.
- (42) Thompson, A. P.; Aktulga, H. M.; Berger, R.; Bolintineanu, D. S.; Brown, W. M.; Crozier, P. S.; in 't Veld, P. J.; Kohlmeyer, A.; Moore, S. G.; Dac Nguyen, T.; Shan, R.; Stevens, M. J.; Tranchida, J.; Trott, C.; Plimpton, S. J. LAMMPS - a flexible simulation tool for particle-based

materials modeling at the atomic, meso, and continuum scales. *Computer Physics Communications* **2022**, *271*, 108171, DOI: [10.1016/j.cpc.2021.108171](https://doi.org/10.1016/j.cpc.2021.108171).

(43) Stukowski, A. Visualization and analysis of atomistic simulation data with OVITO-the open visualization tool. *Modelling and Simulation in Materials Science and Engineering* **2010**, *18*(1), 015012. DOI: [10.1088/0965-0393/18/1/015012](https://doi.org/10.1088/0965-0393/18/1/015012). <https://www.ovito.org/>.

(44) Savitzky, A.; Golay, M. J. E. Smoothing and differentiation of data by simplified least squares procedures. *Analytical Chemistry* **1964**, *36*(8), 1627–1639. DOI: [10.1021/ac60214a047](https://doi.org/10.1021/ac60214a047).

(45) Allen, M. P.; Tildesley, D. J. *Computer Simulation of Liquids (2<sup>nd</sup> ed.)*, Oxford University Press, Oxford, 2017. DOI: [10.1093/oso/9780198803195.001.0001](https://doi.org/10.1093/oso/9780198803195.001.0001).

(46) Ramírez, J.; Sukumaran, S. K.; Vorselaars, B.; Likhtman, A. E. Efficient on the fly calculation of time correlation functions in computer simulations. *Journal of Chemical Physics* **2010**, *133*(15), 154103. DOI: [10.1063/1.3491098](https://doi.org/10.1063/1.3491098).

(47) Doi, Y.; Matsubara, K.; Ohta, Y.; Nakano, T.; Kawaguchi, D.; Takahashi, Y.; Takano, A.; Matsushita Y. Melt rheology of ring polystyrenes with ultrahigh purity. *Macromolecules* **2015**, *48*(9), 3140–3147. DOI: [10.1021/acs.macromol.5b00076](https://doi.org/10.1021/acs.macromol.5b00076).

(48) Doi, Y.; Matsumoto, A.; Inoue, T.; Iwamoto, T.; Takano, A.; Matsushita, Y.; Takahashi, Y.; Watanabe, H. Re-examination of terminal relaxation behavior of high-molecular-weight ring polystyrene melts. *Rheologica Acta* **2017**, *56*, 567–581. DOI: [10.1007/s00397-017-1014-3](https://doi.org/10.1007/s00397-017-1014-3).

(49) Larson, R. G. *The Structure and Rheology of Complex Fluids*, Oxford University Press, Oxford, 1999.

(50) Arrighi, V.; Gagliardi, S.; Dagger, A. C.; Semlyen, J. A.; Higgins, J. S.; Shenton, M. J. Conformation of cyclics and linear chain polymers in bulk by SANS. *Macromolecules* **2004**, *37*(21), 8057–8065. DOI: [10.1021/ma049565w](https://doi.org/10.1021/ma049565w).

(51) Nam, S.; Leisen, J.; Breedveld, V.; Beckham, H. W. Melt dynamics of blended poly(oxyethylene) chains and rings. *Macromolecules* **2009**, *42*(8), 3121–3128. DOI: [10.1021/ma802294j](https://doi.org/10.1021/ma802294j).

(52) Iwamoto, T.; Doi, Y.; Kinoshita, K.; Ohta, Y.; Takano, A.; Takahashi, Y.; Nagao, M.; Matsushita, Y. Conformations of ring polystyrenes in bulk studied by SANS. *Macromolecules* **2018**, *51*(4), 1539–1548. DOI: [10.1021/acs.macromol.7b02358](https://doi.org/10.1021/acs.macromol.7b02358).

(53) Iwamoto, T.; Doi, Y.; Kinoshita, K.; Takano, A.; Takahashi, Y.; Kim, E.; Kim, T.-H.; Takata, S.; Nagao, M.; Matsushita, Y. Conformations of ring polystyrenes in semidilute solutions and in linear polymer matrices studied by SANS. *Macromolecules* **2018**, *51*(17), 6836–6847. DOI: [10.1021/acs.macromol.8b00934](https://doi.org/10.1021/acs.macromol.8b00934).

Supporting Information for “*Identifying the  
Threshold Chain Length for Stress Overshoot in  
Ring/Linear Polymer Blends under Uniaxial  
Elongation: The Role of Multiple Threading*”

*Takahiro Murashima,\*<sup>1</sup> Katsumi Hagita,<sup>2</sup> and Toshihiro Kawakatsu<sup>1</sup>*

<sup>1</sup>Department of Physics, Tohoku University, 6-3, Aramaki-aza-Aoba, Aoba-ku, Sendai, 980-8578, Japan

<sup>2</sup>Department of Applied Physics, National Defense Academy, 1-10-20 Hashirimizu, Yokosuka, 239-8686, Japan

\*[murasima@cmpt.phys.tohoku.ac.jp](mailto:murasima@cmpt.phys.tohoku.ac.jp)

## **S1. Stress Overshoot Behavior under Uniaxial Elongational Flow at a Longer Chain System**

To further validate the chain-length dependence of the stress overshoot, we performed additional simulations for a 1:1 ring-linear blend of flexible chains with  $N = 640$  ( $Z = 8$ ). The simulation methodology and parameters are identical to those described in the Main Text. **Figure S1** shows the transient uniaxial elongational viscosity  $\eta_E(t)$  for this longer chain system. Compared to the  $Z = 4$  case discussed in the Main Text, the  $Z = 8$  system exhibits a more pronounced and sharper stress overshoot at equivalent strain rates. This enhancement is consistent with our hypothesis that an increased number of topological constraints—specifically, a higher degree of threading—leads to greater conformational tension within the rings.

R640:L640=1:1

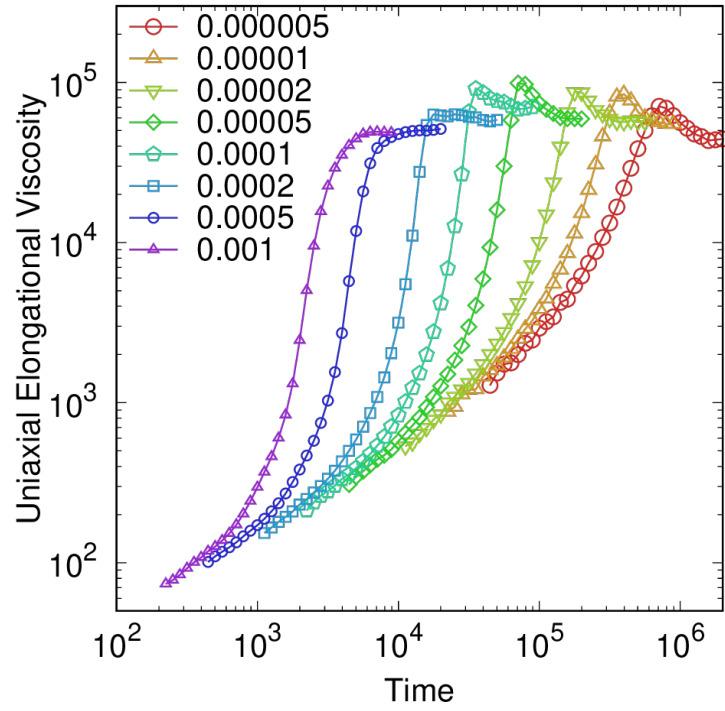


**Figure S1.** Transient uniaxial elongational viscosity  $\eta_E(t) = \{\sigma_{zz}(t) - 0.5[\sigma_{xx}(t) + \sigma_{yy}(t)]\} / \dot{\epsilon}$   $[\tau\epsilon/\sigma^3]$  as a function of time  $t$   $[\tau]$  for a 1:1 ring-linear blend of flexible chains with  $N = 640$  ( $Z = 8$ ) under uniaxial elongational flow. The numerical values denote the applied strain rates,  $\dot{\epsilon}$   $[1/\tau]$ . All physical quantities are expressed in Lennard-Jones (LJ) units.

## S2. Rheological Decomposition of Shorter Chain Blends

To reinforce the identification of the threshold chain length ( $Z \approx 4$ ) discussed in the Main Text, we provide the component-wise stress decomposition for the shorter chain blends, namely, M160 and M80.

**Figure S2** shows the transient first normal stress difference  $N_1 = \sigma_{zz} - 0.5[\sigma_{xx} + \sigma_{yy}]$  for the M160 blend ( $N = 160, Z = 2$ ). While the ring component (**Figure S2b**) exhibits a slight stress overshoot at the higher strain rates, its magnitude is insufficient to induce a clear overshoot in the total stress of the blend (**Figure S2a**). In the total stress response, monotonic growth remains dominant, reflecting a state where the degree of threading is insufficient to sustain high conformational tension across the network.

**Figure S3** shows the results for the M80 blend ( $N = 80, Z = 1$ ). At this chain length, which is near or below the entanglement/threading threshold, no stress overshoot is observed in either the ring or the linear component. Both species exhibit purely monotonic growth toward a steady state (**Figure S3b and c**), confirming that the “thread-to-unthread” transition requires a minimum level of topological constraint that is absent in such short-chain systems.

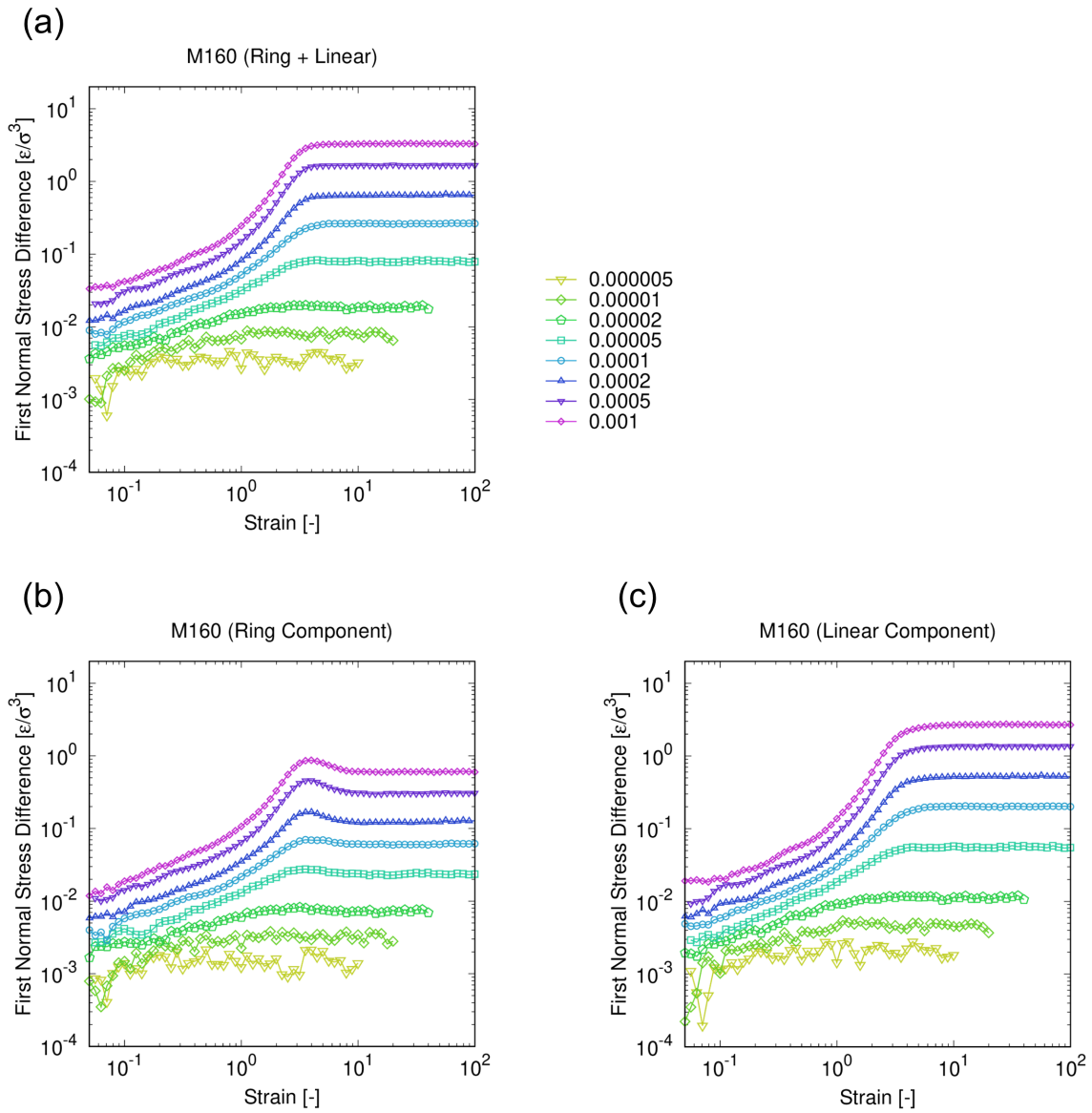


**Figure S2.** Transient first normal stress difference  $N_1 = \sigma_{zz} - 0.5[\sigma_{xx} + \sigma_{yy}]$  as a function of Hencky strain for the M160 blend ( $N=160$ ,  $Z=2$ ) at various strain rates. (a) Total stress of the blend, (b) contribution from the ring component, and (c) contribution from the linear component. While the ring component (b) exhibits a slight stress overshoot at high strain rates, its magnitude is insufficient to induce a clear overshoot in the total stress (a) of the blend, where monotonic growth remains dominant. This contrast with the M320 case highlights the necessity of a higher degree of threading for macroscopic non-linear rheological signatures.

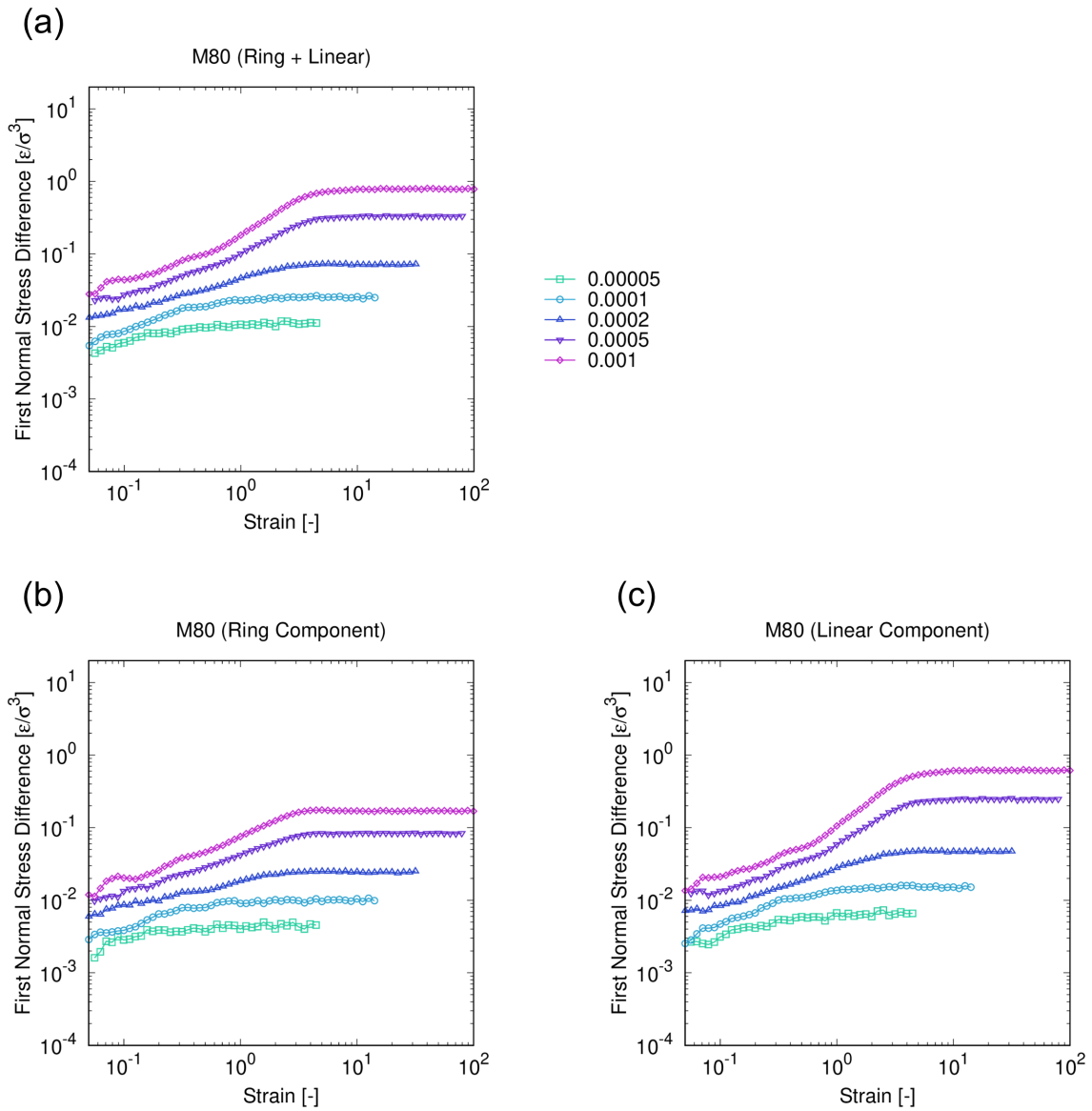


**Figure S3.** Transient first normal stress difference  $N_1 = \sigma_{zz} - 0.5[\sigma_{xx} + \sigma_{yy}]$  as a function of Hencky strain for the M80 blend ( $N=80, Z=1$ ) at various strain rates. (a) Total stress of the blend, (b) contribution from the ring component, and (c) contribution from the linear component. At this chain length (below the entanglement/threading threshold), the stress grows monotonically for both components.

### S3. 1D SANS Profiles and Guinier Plots

To quantitatively evaluate the structural changes under strain, 1D scattering profiles were extracted from the 2D-SANS patterns (**Figure S4**). The profiles along the  $q_{\perp}$  direction were obtained by taking a slice at  $q_z = 0$ , while the profiles along the  $q_z$  direction were obtained at  $q_{\perp} = 0$ . In both ring and linear components in the blend of M320, the  $q_z$  profiles exhibit a rapid decay with increasing strain, indicating structural elongation along the  $z$ -axis.

Guinier analysis was performed on these 1D profiles in the low- $q$  region to determine the components of the radius of gyration. **Figure S5** shows the Guinier plots ( $\ln[I(q)/I(0)]$  vs.  $q^2$ ) for both directions. The linear fits of these plots yielded the values of  $R_{g,z}$  and  $R_{g,\perp}$  as summarized in the legends of **Figure S5** and **Table S1**. It should be noted that for the 1D profiles extracted along the principal axes, the Guinier approximation is expressed as:  $\ln I(q_{\alpha}) \approx \ln I(0) - R_{g,\alpha}^2 q_{\alpha}^2$  ( $\alpha = z, \perp$ ). In contrast to the conventional 3D Guinier law where a factor of  $1/3$  is applied to the total  $R_g^2$ , the factor for these 1D line-cut profiles is unity. This is because the profiles represent the scattering along a specific direction, allowing for the direct determination of the directional components of the radius of gyration,  $R_{g,z}$  and  $R_{g,\perp}$ , from the slopes of the Guinier plots.

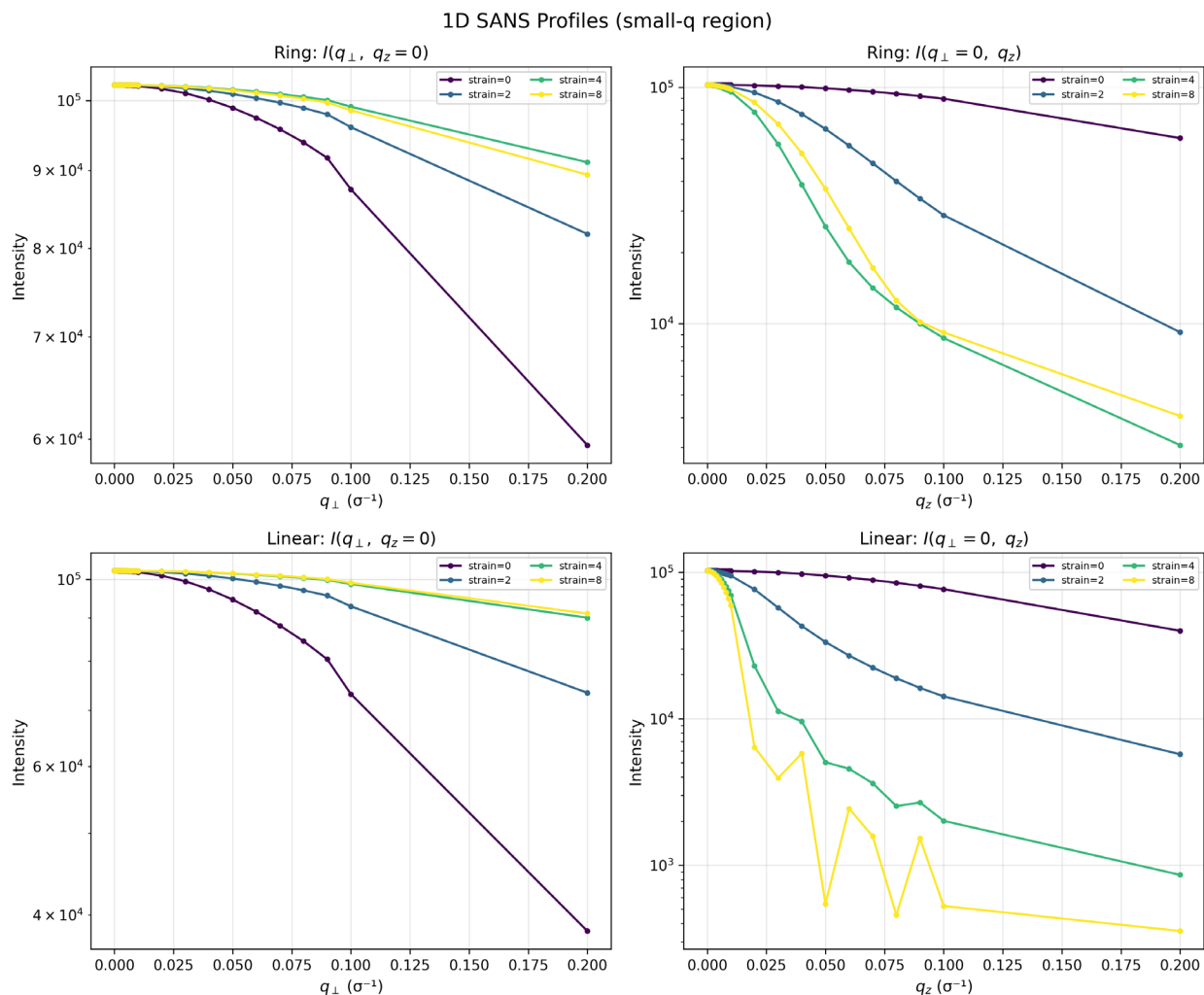


**Figure S4.** 1D SANS intensity profiles in the low- $q$  region. The profiles were extracted from the 2D-SANS patterns for (top) ring and (bottom) linear components in the blend of M320 at various strains ( $\epsilon = 0, 2, 4$ , and  $8$ ). (Left)  $I(q_{\perp}, q_z = 0)$  profiles along the perpendicular direction and (right)  $I(q_{\perp} = 0, q_z)$  profiles along the parallel (elongation) direction.

Guinier Plots

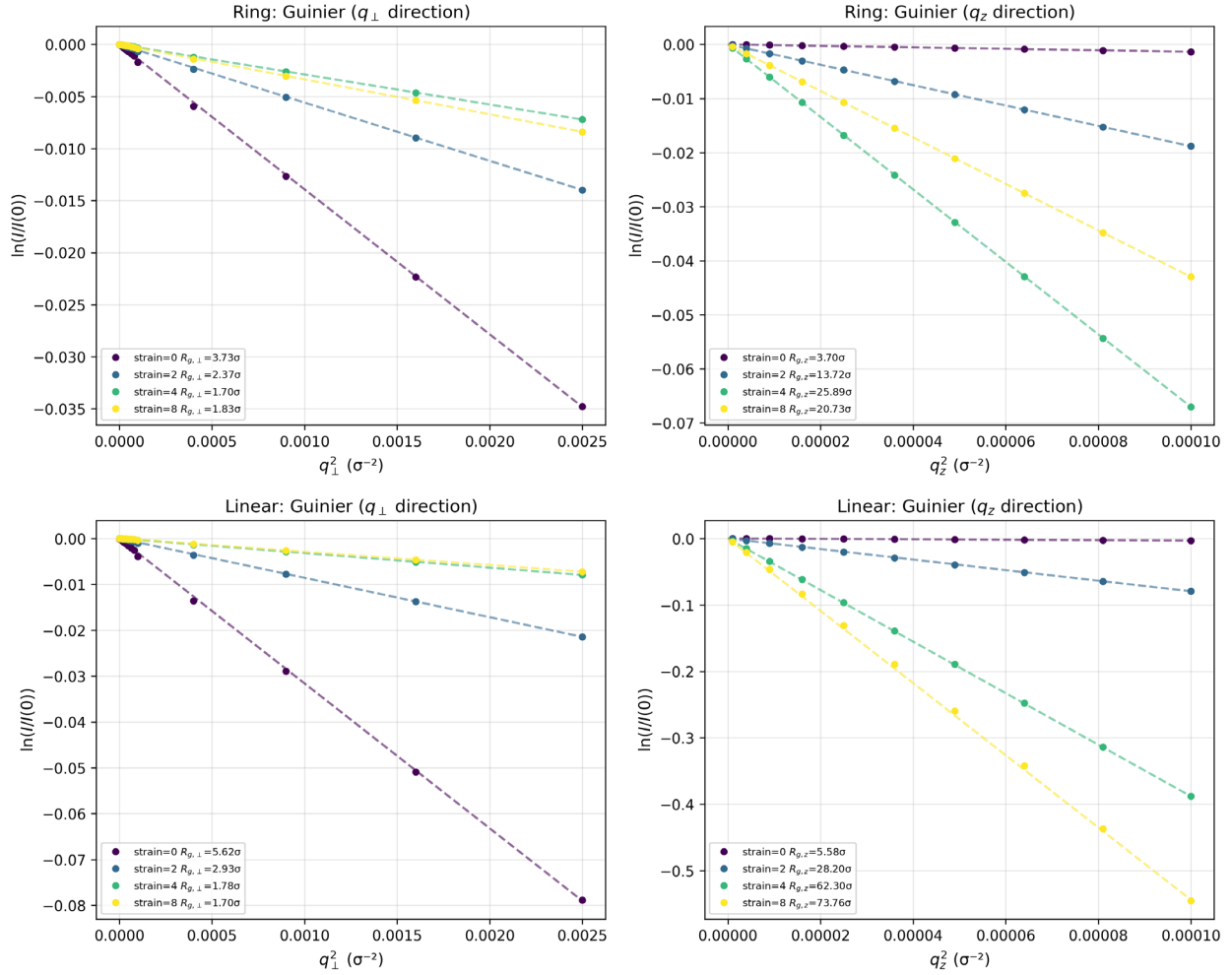


**Figure S5.** Guinier plots extracted from the 1D SANS profiles.  $\ln[I(q)/I(0)]$  is plotted against  $q^2$  for (top) ring and (bottom) linear components in the blend of M320. (Left) Plots for the  $q_{\perp}$  direction and (right) plots for the  $q_z$  direction. The dashed lines represent the linear fits used to determine the directional components of the radius of gyration,  $R_{g,\perp}$  and  $R_{g,z}$ .

**Table S1.** Radius of gyration components along z-axis ( $R_{g,z}$ ) and perpendicular direction ( $R_{g,\perp}$ ) for rings and linear chains in the blend of M320 determined by Guinier analysis. Note that the radius of gyration  $R_g$  is estimated by  $R_g^2 = R_{g,z}^2 + 2R_{g,\perp}^2$ .

	Topology	Strain = 0	Strain = 2	Strain = 4	Strain = 8
$R_g$	Ring	$6.4\sigma$	$14.1\sigma$	$26.0\sigma$	$20.8\sigma$
	Linear	$9.7\sigma$	$28.5\sigma$	$62.3\sigma$	$73.7\sigma$
$R_{g,z}$	Ring	$3.6\sigma$	$13.7\sigma$	$25.8\sigma$	$20.7\sigma$
	Linear	$5.5\sigma$	$28.1\sigma$	$62.3\sigma$	$73.7\sigma$
$R_{g,\perp}$	Ring	$3.7\sigma$	$2.3\sigma$	$1.7\sigma$	$1.8\sigma$
	Linear	$5.6\sigma$	$2.9\sigma$	$1.7\sigma$	$1.7\sigma$